Glacial erosion and history of Inglefield Land, northwest Greenland

Submitted to: *The Cryosphere*

Caleb K. Walcott-George[1], Allie Balter-Kennedy[2], Jason P. Briner[1], Joerg M. Schaefer[2], Nicolás E. Young[2]

[1]Department of Geology, University at Buffalo, Buffalo, NY 14260, USA
[2]Lamont-Doherty Earth Observatory, Columbia University, Palisades, NY 10964, USA

Correspondence to: Caleb Walcott-George (ckwalcot@buffalo.edu)

Abstract:

We used mapping of bedrock lithology, bedrock fractures, and lake density in Inglefield Land, northwest Greenland, combined with cosmogenic nuclide (^{10}Be and ^{26}Al) measurements in bedrock surfaces, to investigate glacial erosion and the ice-sheet history of the northwestern Greenland Ice Sheet. The pattern of eroded versus weathered bedrock surfaces and other glacial erosion indicators reveal temporally and spatially varying erosion under cold- and warm-based ice. All of the bedrock surfaces that we measured in Inglefield Land contain cosmogenic nuclide inheritance with apparent ^{10}Be ages ranging from 24.9 ± 0.5 to 215.8 ± 7.4 ka. The ^{26}Al/^{10}Be ratios require minimum combined surface burial and exposure histories of ~150 to 2000 kyr. Because our sample sites span a relatively small area that experienced a similar ice-sheet history, we attribute differences in nuclide concentrations and ratios to varying erosion during the Quaternary. We show that an ice sheet history with ~900 kyr of exposure and ~1800 kyr of ice cover throughout the Quaternary is consistent with the measured nuclide concentrations in most samples when sample-specific subaerial erosion rates are between 0 and 2 x 10^{-2} mm yr^{-1} and subglacial erosion rates are between 0 and 2 x 10^{-3} mm yr^{-1}. These erosion rates help to characterize Arctic landscape evolution in crystalline bedrock terrains in areas away from focused ice flow.

1. Introduction

The Greenland Ice Sheet currently contributes more to sea level rise than any other single ice mass and is predicted to continue to melt at an accelerated rate throughout the next century (e.g., Aschwanden and Brinkerhoff, 2022; Goelzer et al., 2020). Ice sheet models used to predict future ice sheet evolution are aided by the knowledge of long-term ice sheet history and patterns of past ice flow variability, as these play a large role in modulating ice sheet mass balance (e.g., Hubbard et al., 2009). Uncertainty in ice-sheet model parameters can be narrowed when paleo-ice-sheet simulations are performed alongside geologic constraints (e.g., Briner et al., 2020; Cuzzone et al., 2016; Patton et al., 2017). Observations of many ice-sheet processes are sparse because it is difficult to access the bed of modern ice sheets; thus, investigating the beds of former ice sheets (i.e., glaciated landscapes) provides information on past ice sheet dynamics and basal processes such as glacial erosion.

The distribution of glacial erosional features including striations, lakes, lateral meltwater channels, and sculpted bedrock across glaciated landscapes at ice-sheet scale has been used to map past basal thermal conditions and relative ice velocities delineating zones of warm-bedded and/or fast flowing ice where erosional features are abundant, from areas of cold-based ice and ancient (Quaternary/pre-Quaternary) landscape preservation where these features are absent (Andrews et al., 1985; Daly, 1902; Flint, 1943; Margold et al., 2015; Sugden, 1978). Identifying areas of differential erosion in glaciated landscapes is particularly useful for mapping paleo-ice streams, as knowing their extent is helpful for understanding the mass balance of former ice sheets through ice sheet models. Ice streams play a large role in modulating the volume of the modern Greenland Ice Sheet, and their stability is directly linked to overall ice sheet mass balance (e.g., Khan et al., 2022; Mouginot et al., 2015). These features are large areas of fast-moving ice, with onset zones

53   that feed into main channels, which eventually calve into the ocean and are constrained by

54   topography or slow-moving ice (Benn and Evans, 2010). Paleo-ice stream onset zones (i.e., the

55   head of ice streams) are found at the transitions between warm-and cold-based ice, which can be

56   delineated via mapping of erosion imprints on a landscape and cosmogenic nuclide analysis

57   (Briner et al., 2008; Margold et al., 2015, 2018).

58   Cosmogenic nuclides are produced mostly in the upper few meters of the Earth's surface

59   when it is exposed to the cosmic ray flux and are routinely used in glaciated landscapes to quantify

60   erosion rates and the timing of past ice sheet fluctuations (Gosse and Phillips, 2001). In areas

61   covered by warm-based, highly erosive glaciers, nuclides that have accumulated in the upper 2-3

62   meters of bedrock are often removed through efficient glacial erosion. In areas of minimal-to-no

63   glacial erosion (i.e., covered by cold-bedded glaciers or short-lived erosive ice), bedrock surfaces

64   contain inventories of cosmogenic nuclides from multiple periods of exposure (known as

65   cosmogenic nuclide inheritance; Bierman et al., 1999). Patterns of inheritance (or lack thereof)

66   across a landscape can be used to delineate ice streaming where faster flowing, erosive ice depleted

67   nuclide inventories (Briner et al., 2006; Corbett et al., 2013; Roberts et al., 2013).

68   Cosmogenic nuclide inheritance resulting from minimal glacial erosion can pose an issue

69   for single nuclide surface exposure dating, where the apparent exposure age will be anomalously

70   old (Ivy-Ochs and Briner, 2014). However, some cosmogenic nuclides are radioactive and decay

71   when they are shielded from the cosmic ray flux by ice (e.g., ^{10}Be, ^{26}Al; no significant production

72   beneath tens of meters of ice; Miller et al., 2006). The production ratio of ^{26}Al/^{10}Be is 7.3:1 in

73   quartz at the Earth's surface across Greenland (Corbett et al., 2017). Because ^{26}Al has a shorter

74   half-life (705 kyr) than ^{10}Be (1388 kyr), departure from this ratio indicates surface burial

75   (Korschinek et al., 2010; Nishiizumi, 2004). By measuring multiple nuclides in bedrock surfaces

76 near the modern Greenland Ice Sheet margin, researchers have exploited cosmogenic nuclide

77 inheritance to investigate periods of ice sheet minima, glacial erosion, and longer-term ice sheet

78 history (e.g., Corbett et al., 2013; Skov et al., 2020; Young et al., 2021).

79   Recently, attention has been drawn to retrieving samples from the bed of modern extant

80 ice sheets (i.e., Greenland and Antarctic ice sheets; Briner et al., 2022; Johnson et al., 2024; Spector

81 et al., 2018). The information contained at the contemporary ice-bed interface provides valuable,

82 and rare, terrestrial constraints on previous ice sheet minima and long-term ice sheet history.

83 Cosmogenic nuclide and luminescence analysis of sediment and bedrock samples collected from

84 the modern glacier bed have provided insight into the stability of the ice sheet throughout the

85 Quaternary (Balco et al., 2023; Bierman et al., 2023; Christ et al., 2020; Christ et al., 2021; Christ

86 et al., 2023; Schaefer et al., 2016). Studying the landscape at the fringes of the Greenland Ice Sheet

87 allows us to systematically investigate large areas of the former ice sheet bed, without the need to

88 drill through the ice sheet, providing complementary results for efforts focused on obtaining

89 material from under the ice. We mapped bedrock features and used cosmogenic nuclide analysis

90 to determine the extent and magnitude of erosion and the ice sheet history across Inglefield Land,

91 northwest Greenland over the Quaternary.

92

93 **2. Inglefield Land**

94 Inglefield Land is an ice-free area in northwest Greenland situated between the Greenland Ice

95 Sheet and the coastline 30 km to the northwest. It is bounded by Smith Sound to the west, Kane

96 Basin to the north, Prudhoe Dome and the main body of the northern Greenland Ice Sheet to the

97 south, and the Hiawatha Glacier sector of the Greenland Ice Sheet to the east (Fig. 1). Today, much

98 of the ice bordering Inglefield Land is cold based, and ice velocities are low, ranging from 10 m

99   yr^{-1} to ~120 m yr^{-1} (Fig. 1; Joughin et al., 2018; MacGregor et al., 2022). Inglefield Land is

100 characterized by relatively low-relief uplands that reach 700 m asl near the ice margin with valleys

101 incised along the northern coast. Ice sheet meltwater drains into through these valleys and into four

102 embayments (from west to east): Force Bay, Rensselaer Bay, Marshall Bay, and Dallas Bay

103 (henceforth the unnamed valleys crossing Inglefield Land will be referred to by the bays into which

104 they drain).

105   During the Last Glacial Maximum (LGM; 26 – 19 ka), the northern Greenland Ice Sheet

106 covered Inglefield Land completely as it advanced into Kane Basin, where it coalesced with the

107 Innuitian Ice Sheet and flowed southward, eventually terminating in an iceshelf spanning northern

108 Baffin Bay (England, 1999; Couette et al., 2022; Batchelor et al., 2024). Although the timing and

109 duration of the LGM ice advance remains unknown, retreat onto the modern coast of Inglefield

110 Land is constrained to ~8.6 – 7.9 ka based on radiocarbon dating of organic material in raised

111 beach deposits and *in-situ* ^{14}C ages from erratic boulders (Blake et al., 1992; Mason, 2010; Nichols,

112 1969; Søndergaard et al., 2020). The ice sheet continued to decay, arriving at the modern margin

113 by ~7 ka and maintaining smaller-than-modern position between ~5.8 and 0.3 ka, an estimate

114 based on radiocarbon ages from reworked wood fragments at the modern ice margin (Søndergaard

115 et al., 2020).

116   The pre-Holocene ice-sheet history and dynamics of Inglefield Land is not known, though

117 cosmogenic nuclide inheritance (^{10}Be) found in boulders across Inglefield Land indicates that

118 much of the landscape was covered by cold-based ice during the last glacial cycle (Søndergaard et

119 al., 2020). Limited ice sheet-scale terrestrial records suggest that there were major deglaciation

120 events during the Quaternary as captured by cosmogenic nuclide and luminescence analysis of

121 sub-ice sediment and bedrock at Camp Century and Summit, during which Inglefield Land was

122 almost certainly ice free (Christ et al., 2021; Christ et al., 2023; Schaefer et al., 2016). Additionally,

123 offshore marine sediment records imply that the ice sheet underwent several cycles of advance and

124 retreat, though inland extent of ice-sheet recession in North Greenland during interglacials is

125 poorly constrained (Bierman et al., 2016; Colville et al., 2011; Hatfield et al., 2016; Knutz et al.,

126 2019; Reyes et al., 2014).

127

128

129 **3 Methods**

130 We used mapping, field observations, ^{10}Be and ^{26}Al measurements from bedrock surfaces at eleven

131 sites to assess the ice sheet history and erosive conditions of the northwestern Greenland Ice Sheet

132 across Inglefield Land. Mapping and field observations allowed us to broadly identify variable

133 subglacial and subaerial erosion across the landscape, while cosmogenic nuclide measurements

134 helped us quantify ice-sheet history and erosion.

135

136 ***3.1 Geologic mapping – GIS and field observations***

137 *3.1.1 Bedrock lithology*

138 The relatively simple bedrock geology of Inglefield Land allowed us to investigate the long-term

139 pattern of erosion and landscape evolution of the area using pre-existing geologic maps. Inglefield

140 Land is underlain by crystalline paragneiss and capped with near-horizontally bedded sedimentary

141 rocks; therefore, generally speaking, outcrops of basement rock indicate areas where cap rocks

142 have been removed by erosion (Fig. 2). Some of this cap rock removal likely took place prior to

143 Quaternary glaciation (e.g., Krabbendam and Bradwell, 2014), but the patterns seen in the geologic

144 map – with crystalline lithologies in glacial troughs – hints at the role of past glacial erosion in

145 shaping the landscape. To identify the removal of sedimentary cap rocks, we created a simplified

146 geologic map of Inglefield Land using the 1:500,000 Greenland-wide geologic map in ArcGIS Pro

147 (Kokfelt et al., 2023) and classified units as crystalline, sedimentary, Quaternary sediments or

148 lakes. In the field, we noted the lithology at each of our sample sites and whether bedrock outcrops

149 exhibited evidence of ice sculpting (e.g., sculpted bedrock, striations, glacial polish) or weathering

150 (e.g., grussification, weathering pits; Figs. 2, 3).

151

152 *3.3.2 Mapping bedrock fractures*

153 Bedrock fractures in glaciated terrains are exposed through the removal of regolith by glacial

154 erosion (Gordon, 1981; Skyttä et al., 2023; Sugden, 1974, 1978). Areas with a high density of

155 exposed bedrock fractures within crystalline bedrock areas have been used to identify intense

156 glacial erosion (e.g., Sugden, 1978). This is in contrast to areas where bedrock fractures are

157 obscured by sediment cover, a regolith mantle, or in some cases, sub-horizontal sedimentary

158 bedrock units. Our field area has a heterogenous pattern of mappable fractures that are easily

159 identifiable at the landscape-level (>25 m), indicative of areas where regolith has been stripped

160 via glacial erosion. We outlined zones of bedrock fractures at the landscape scale in ArcGIS Pro

161 using a 25 m resolution digital elevation model (Korsgaard et al., 2016). We created hillshade

162 images with a three-times vertical exaggeration for our mapping (Fig. 4). Our digital elevation

163 model resolution of 25 m was fine enough to capture areas of obvious bedrock fractures on a

164 landscape scale, but coarse enough to avoid mistaking smaller fractures for other landscape

165 features.

166

167

168

169   *3.3.3 Mapping lake density*

170   Lake density has also been used as a proxy for glacial erosion (e.g., Andrews et al., 1985; Briner

171   et al., 2008; Sugden, 1978). Areas of regolith cover are generally topographically smooth on the

172   landscape-scale and contain few lakes. Meanwhile, areas of high erosion rates beneath ice sheets

173   can remove this overlying regolith and expose the underlying bedrock, after which the bedrock is

174   susceptible to ice sheet scouring and erosion. These bedrock basins then fill with water following

175   glacial retreat forming lakes across glaciated areas and thus, the density of lakes can be used as an

176   indicator of past ice sheet erosion. We created an inventory of lakes in Inglefield Land to calculate

177   lake density. While the 1:500,000 geologic map of Greenland shows larger lakes, smaller lakes are

178   not included due to the relatively coarse map resolution (Fig. 2; Kokfelt et al., 2023). Therefore,

179   we used a semi-automated process in ArcGIS Pro to map all lakes in the study area. First, we used

180   cloud-free LANDSAT8 images to visualize surface water (Band 5; visible blue-green). We

181   explored a range of threshold values to extract cells with surface water from this image (Fig. 5;

182   cells with a value less than the threshold of 8000 were water, though we note this value may not

183   be suitable for any location) and evaluated these against the original LANDSAT8 images to

184   determine a suitable threshold value that adequately captured lakes and streams. We converted this

185   raster to polygons of lake and river extents. Finally, we conducted manual quality control by

186   removing rivers and any lakes that were by ice sheets and then merged our new lake polygons with

187   those from the geologic map. To calculate lake density across Inglefield Land, we determined the

188   percentage of each cell in a 1 x 1 km grid covered by lake polygons.

189

190

191

192   ***3.4 Cosmogenic nuclide measurements***

193   *3.4.1 Sampling approach*

194   We collected samples for cosmogenic nuclide measurements from bedrock surfaces along two

195   SSE – NNW transects from the ice margin to the coast in Inglefield Land (Figs. 1; Table S1). We

196   sampled roughly one kg of crystalline rock from 15 bedrock surfaces and one boulder using a

197   handheld angle grinder, hammer, and chisel during summer 2022. We collected nine samples along

198   our western transect (beginning at the mouth of Rensselaer Valley): two from bedrock surfaces

199   and one from a boulder (2.5 m long x 1.6 m wide x 1.1 m tall) close to the ice margin, one bedrock

200   sample from each of three separate inland sites, one bedrock sample from a higher-elevation

201   coastal site (255 m asl), and two bedrock samples from a lower-elevation coastal site (~100 m asl).

202   Along our eastern transect (beginning at the mouth of western Marshall Valley), we collected

203   bedrock samples: three from near the ice margin, one sample from each of three different inland

204   sites, and one sample from a low-elevation coastal site (~100 m asl).

205

206   *3.4.2 Lab procedures*

207   We measured ^{10}Be and ^{26}Al in all 16 of our samples. We isolated quartz and extracted ^{10}Be and

208   ^{26}Al at the University at Buffalo Cosmogenic Isotope Laboratory (n = 12) and the Lamont-Doherty

209   Earth Observatory (LDEO) cosmogenic dating laboratory (n = 4) using well-established

210   procedures (Corbett et al., 2016b; Kohl and Nishiizumi, 1992). We spiked our dissolved samples

211   with precisely weighed ^{9}Be carrier (PRIME Lab 2017.11.17-Be #3/#4 – ^{9}Be concentration of 1074

212   ± 8 ppm – at the University at Buffalo and LDEO carrier – ^{9}Be concentration of 1038.8 ppm – at

213   LDEO). We measured the amount of native ^{27}Al in our dissolved quartz and added varying

214   amounts of ^{27}Al carrier to ensure each sample had ~2000 mg of ^{27}Al. We measured the total amount

215   of ^{27}Al in aliquots removed after sample digestion with inductively coupled plasma optical

216   emission spectrometry. We sent ^{10}Be samples processed at the University at Buffalo and all ^{26}Al

217   samples to PRIME Lab and ^{10}Be samples processed at Lamont-Doherty to Lawrence-Livermore

218   National Laboratory, where the ^{10}Be/^{9}Be and ^{26}Al/^{27}Al ratios were measured by accelerator mass

219   spectrometry.

220   ^{10}Be/^{9}Be ratios were measured relative to the 07KNSTD standard (^{10}Be/^{9}Be ratio: 2.85 x

221   10^{-12}; Nishiizumi et al., 2007) at both facilities and ^{26}Al samples relative to the KNSTD standard

222   (^{26}Al/^{27}Al ratio: 1.82 x 10^{-12}; Nishiizumi, 2004). Analytical uncertainties (1σ) of ^{10}Be

223   measurements at Lawrence Livermore were between 1.8% and 1.9% and ranged from 1.5% to

224   6.0%, with an average of 2.6 $\pm$ 1.3% at PRIME lab. ^{26}Al measurement uncertainties ranged from

225   3.6% to 8.4% with an average of 4.8 $\pm$ 1.5%. We applied background corrections to both ^{10}Be and

226   ^{26}Al sample ratios using batch-specific process blank values (Table S1).

227   We calculated apparent exposure ages using version 3 of the online exposure age calculator

228   from Balco et al. (2008). We used the Arctic ^{10}Be production rate, with a time-independent 'St'

229   production rate scaling method to calculate apparent exposure ages (Lal, 1991; Stone, 2000; Young

230   et al., 2013). We did not include production rate uncertainties in our exposure age calculations

231   because we do not compare our age results to other independent dating methods. We used a

232   Greenland-specific ^{26}Al/^{10}Be surface production ratio in quartz of 7.3 for interpreting

233   exposure/burial histories from both nuclides (Corbett et al., 2017).

234

235   *3.5 Modeling cosmogenic nuclide accumulation in rock surfaces*

236   In bedrock samples with cosmogenic nuclide inheritance, measurements of two isotopes with

237   different half-lives have been used to calculate Greenland Ice Sheet exposure and burial histories

238   (e.g. Andersen et al., 2020; Beel et al., 2016; Corbett et al., 2013; Knudsen and Egholm, 2018;

239   Knudsen et al., 2015; Skov et al., 2020; Strunk et al., 2017). Although *in-situ* [14]C ages from

240   boulders constrain ice retreat across Inglefield Land to between ~9 and 7 ka, apparent [10]Be ages

241   from boulders date to between 8.3 ± 1.2 and 92.7 ± 1.5 ka, indicating the presence of nuclide

242   inheritance (Søndergaard et al., 2020). Inglefield Land bedrock also is likely to contain nuclide

243   inheritance and therefore yield information about ice sheet history and erosion prior to the last

244   glacial cycle. Given the relatively small distance from the modern ice margin to coast (<50 km)

245   and the speed at which Inglefield Land deglaciated following the LGM (<2 kyr), we hypothesize

246   that, within [10]Be and [26]Al measurement uncertainties, the 15 bedrock samples should have similar

247   ice-cover histories on glacial-interglacial timescales (Søndergaard et al., 2020). Therefore,

248   differences in [10]Be and [26]Al concentrations across the landscape likely relate to varying sample-

249   to-sample sub-glacial and sub-aerial erosion rates and not differences in ice-sheet history at each

250   sample location..

251   To explore this hypothesis, we simulate complex Pleistocene exposure histories using a

252   forward model that calculates cosmogenic [10]Be and [26]Al accumulation in rock brought to the

253   Earth's surface by subaerial and subglacial erosion. Because little is known about the ice-margin

254   history in Inglefield Land prior to the Holocene, we define the pre-Holocene exposure/burial

255   history by applying a threshold value on the benthic δ^{18}O LR04 stack (Lisiecki and Raymo, 2005)

256   to define a range of plausible exposure/burial scenarios for the last 2.7 Myr, following the approach

257   adopted in prior studies (Balter-Kennedy et al., 2021; Knudsen et al., 2015). Exposure and burial

258   take place at δ^{18}O values below and above the threshold, respectively. We use a 30 kyr running

259   mean to smooth the δ^{18}O curve (Knudsen et al., 2015). Given the prevalence of nuclide inheritance

260   across Inglefield Land (Søndergaard et al., 2020), we do not expect [10]Be to give post-LGM

261   deglaciation ages at each sample location, but deglaciation ages from *in situ* [14]C in boulders at the

262   coast and ice margin are provided by Søndergaard et al. (2020). We therefore estimate site-specific

263   Holocene exposure durations by scaling the deglaciation ages from Søndergaard et al. (2020) to

264   each of our sites based on their relative distance between the coast and ice margin, as calculated

265   along our sample transects. This Holocene-exposure scaling does not account for variability in

266   Holocene lateral retreat rates. Ultimately, however, the goal of this exercise is to determine

267   whether a long-term exposure history can explain the measured cosmogenic nuclide

268   concentrations, which is not drastically affected by slight variations in the Holocene exposure

269   history.

270   The cosmogenic-nuclide concentration (atoms g^{-1}), N, for nuclide, i, at the end of each

271   timestep, j, is the sum of nuclides inherited from the previous timestep (adjusted for radioactive

272   decay) and the new accumulation of nuclides (assumed zero when ice covered and limited by the

273   surface erosion rate when ice free):

274

275
$$N_{i,j} = N_{i,j-1}e^{-\lambda_i t_j} + \int_0^{t_j} P_i(z_{end,j} + \varepsilon_j \tau)e^{-\lambda_i \tau}d\tau$$

276

277   where λ is the decay constant (5.00 x 10^{-7} for [10]Be; 9.83 x 10^{-7} for [26]Al; (Korschinek et al., 2010;

278   Nishiizumi, 2004) and t_j is the duration of the timestep (yrs). P_i is the sum of nuclide production

279   (atoms g^{-1} yr^{-1}) by spallation and muon interactions at a given mass depth (g cm^{-2}). Here, mass

280   depth is time-varying, controlled by subaerial and subglacial erosion during ice-free and ice-

281   covered timesteps, respectively. Therefore, the mass depth is defined by the sample depth at the

282   end of each timestep, $z_{end,j}$, and the erosion rate (g cm^{-2} yr^{-1}), ε_j, during that timestep. We calculate

283   spallation production rates at the Earth's surface using the Arctic [10]Be calibration dataset of Young

284   et al. (2013), a [26]Al/[10]Be ratio of 7.3 (Corbett et al., 2017; Young et al., 2021), and the scaling

285   method of Stone (2000). We assume spallation production decreases exponentially with mass

286   depth at an attenuation length of 160 g cm^{-2}. We calculate production by muon interactions in

287   MATLAB using the cross sections for ^{10}Be and ^{26}Al determined by Balco (2017) and implemented

288   in Model 1A in the same reference.

289   We determine the misfit between the modeled and measured nuclide concentrations for

290   each sample, d, using the error-weighted sum of squares (EWSS):

291
$$EWSS = \left(\frac{N_{10,p,d} - N_{10,m,d}}{\sigma_{10,m,d}}\right)^2 + \left(\frac{N_{26,p,d} - N_{26,m,d}}{\sigma_{26,m,d}}\right)^2$$

292

293   where $N_{i,p,d}$ is the predicted nuclide concentration, $N_{i,m,d}$ is the measured nuclide concentration, and

294   $\sigma_{i,m,d}$ is the 1σ measurement uncertainty. An error-weighted sum of squares close to two indicates

295   that the difference between the modeled and measured concentrations can be explained by the

296   measurement uncertainty. We consider model runs with an error-weighted sum of squares less

297   than 2.5 to be acceptable fits.

298   We created 2.7-Myr exposure histories using δ^{18}O threshold values ranging from 3.60 to

299   4.00‰ (corresponding to 0.7–1.9 Myr cumulative exposure and 0.8–2 Myr cumulative burial over

300   the last 2.7 Myr) at 0.02‰ spacing. We decouple this δ^{18}O threshold-based exposure timing during

301   Holocene deglaciation (Knudsen et al., 2015), as the timing of Holocene exposure is relatively

302   well-known from the constraints from Søndergaard et al. (2020). For each exposure history, we

303   ran the forward model with subaerial and subglacial erosion rates ranging from 0 to 2.5 x 10^{-1} mm

304   yr^{-1} on a log scale (coarse spacing from 0 to 1 x 10^{-5} mm yr^{-1} and finer spacing from 1 x 10^{-5} to 2.5

305   x 10^{-1} mm yr^{-1}) to capture the potential range in subglacial erosion rates for cold-bedded glaciers

306   and subaerial erosion rates polar environments (e.g., Cook et al., 2020; Koppes et al., 2015;

307   Portenga and Bierman, 2015). Subglacial and subaerial erosion rates are each held constant for all

308   periods of ice cover and exposure, respectively, and therefore we do not consider changes in

309   erosion within glacial cycles or from one glacial cycle to the next. If total (subaerial + subglacial)

310   erosion through a model run is high, a higher proportion of modeled ^{10}Be and ^{26}Al accumulates

311   deep in the rock column where production is low, while less erosion results in a larger fraction of

312   the nuclide production near the surface where production is higher. The two erosion rates may

313   therefore trade-off. For example, an exposure history may yield a good fit to the data with a higher

314   sub-aerial erosion rate and lower sub-glacial erosion rate for a certain sample, as well as with a

315   lower sub-glacial erosion rate and a higher sub-aerial erosion rate. Thus, this model allows us to

316   investigate potential Quaternary erosion and ice cover scenarios across Inglefield Land to test the

317   hypothesis that the variability in our cosmogenic nuclide measurements can be explained with a

318   common 2.7 Myr exposure-burial history and sample-specific subaerial and subglacial erosion

319   rates.

320

321   **4 Results**

322   *4.1 Mapping*

323   Paleoproterozoic crystalline paragneiss basement rocks are overlain by sub-horizontally bedded

324   Mesoproterozoic to Ordovician sedimentary rocks across Inglefield Land (Fig. 2). Near the ice

325   margin, crystalline basement rocks are exposed, with some areas covered by Quaternary

326   sediments. Along much of the coastline of Inglefield Land, sedimentary rock units extend up to 20

327   km inland, except where erosion incised the cap rock to expose the underlying basement rocks in

328   the four main valleys. North of Hiawatha Glacier, crystalline basement outcrops from the ice

329   margin to the coastline. In total, 48.2% of the surface of Inglefield Land is crystalline basement,

330   29.4% is sedimentary cap rocks, and 17.4% is Quaternary sediments, with the remaining 5% made

331   up of lakes and minor geologic units.

332   The low-elevation coastal (~100 m asl) sites exhibit ice-sculpted bedrock with primary

333   glacial erosional features, including striations (Fig. 3). Smoothed bedrock is also present at the

334   higher-elevation coastal site (255 m asl), though it lacked primary glacial erosional features such

335   as striations or glacial polish. Inland, highly weathered bedrock outcrops, often with abundant

336   gruss, rose only a few meters above the surrounding landscape, which is covered by Quaternary

337   sediments composed of weathered, angular boulders. Near the ice margin sites, we also found

338   highly weathered bedrock outcrops exhibiting lots of gruss and weathering pits on rock surfaces.

339   Exposed bedrock fractures are sparse across Inglefield Land, except for the areas west and

340   north of Hiawatha glacier where bedrock fractures are clearly visible at the kilometer-scale, as

341   mapped in Fig. 4. There are sizable fracture zones along Rensselaer Valley and both Marshall

342   valleys; in particular, the fracture zone of the western Marshall Valley extends ~25 km inland.

343   Finally, there are some limited fracture areas in the central inland sector towards the ice sheet.

344   Lakes are abundant across much of Inglefield Land, covering 161 km^2, (2% of the surface

345   area), but are concentrated in certain sectors (Fig. 6). Regions to the west and north of Hiawatha

346   Glacier have the highest lake densities, with some 1 km^2 cells 87% covered by lakes. There are

347   also areas of high lake densities towards the coast, particularly near the coastal valleys. Inland, the

348   highest density of lakes is found in central Inglefield Land. Many grid cells do not contain lakes

349   (grid cells not filled in on Fig. 6), or host very small lakes (<1% of grid cell is lake-covered).

350   Taken together, there are clear areas of overlap between exposed crystalline basement rock,

351   bedrock fractures, and high lake densities north of Hiawatha Glacier and in the valleys draining

352   into Rensselaer and Marshall bays (Fig. 7). West of Hiawatha Glacier and in western Inglefield

353   Land, there are large areas of exposed basement rocks with lakes, but no large-scale fractures.

354   There are also a few areas of sedimentary cap rock with high lake densities, most notably between

355   Rensselaer, Marshall, and Dallas bays.

356

357   *4.2 Cosmogenic nuclide analysis*

358   Apparent [10]Be exposure ages are generally youngest at our coastal sites and oldest at inland sites.

359   [10]Be concentrations are lowest at our ~100 m asl coastal sites, corresponding to apparent exposure

360   ages between 24.9 ± 0.5 and 36.5 ± 1.7 ka (Figs. 7 & 8; Table S1). These sites exhibit evidence of

361   glacial erosion including sculpted bedrock and striations, suggesting the presence of warm-based

362   ice. At the higher elevation coastal site on the western transect (255 m asl), the apparent [10]Be age

363   is slightly older – 62.2 ± 1.7 ka. Our oldest apparent exposure ages come from the inland sites on

364   both transects, dating from 99.1 ± 2.4 ka to 213.7 ± 3.5 ka on the western and 87.9 ± 3.8 ka to

365   215.8 ± 7.4 ka on the eastern transects. We do not observe any relationship between the apparent

366   [10]Be exposure age of our inland sites and their elevation or distance along the transect. Ages from

367   the ice margin sites generally fall between those from the coast and inland sites. Apparent [10]Be

368   exposure ages from the western ice margin site range from 50.2 ± 0.9 ka to 133.7 ± 2.6 ka. At the

369   eastern ice margin site, [10]Be ages are between 49.2 ± 0.9 ka and 62.6 ± 1.2 ka. Our single boulder

370   sample at the western ice margin site has an apparent [10]Be exposure age of 50.2 ± 0.9 ka.

371   [26]Al/[10]Be ratios follow a general inverse pattern to the apparent [10]Be ages, with the highest

372   ratios (closest to the production ratio) at the coast, lowest ratios inland, and ratios from the ice

373   margin in the middle. At the coastal sites, the three samples taken from ~100 m asl have ratios of

374   6.38 ± 0.44, 7.58 ± 0.42, 8.41 ± 0.81 and overlap with the constant exposure isochron with 95%

375   confidence (Fig. 9). The 255 m asl coastal site has a ratio of 5.68 ± 0.30 requiring a minimum

376   burial duration of 500 kyr and at least 25–100 kyr of exposure. In contrast, ^{26}Al/^{10}Be ratios at our

377   inland sites range from 2.19 ± 0.16 to 5.28 ± 0.30, with the majority falling between the 500 and

378   1500 kyr burial isochrones and between the 100 and 500 kyr exposure isochrones for total

379   minimum exposure and burial durations of between ~600 and ~2000 kyr. There is one apparent

380   outlier below the 2000 kyr burial isochron with a ratio of 2.19± 0.16 (22GRO-03). At the western

381   ice margin site, ^{26}Al/^{10}Be ratios in our three samples range between 4.00 ± 0.18 and 5.14 ± 0.21,

382   corresponding to a minimum glacial history with ~100 and ~250 kyr of cumulative exposure and

383   ~250 – ~1250 kyr of cumulative burial. The boulder has a ^{26}Al/^{10}Be ratio of 5.15 ± 0.21, which is

384   the highest ratio at the western ice margin site. At the eastern ice margin site, ^{26}Al/^{10}Be ratios are

385   between 5.11 ± 0.21 and 5.53 ± 0.26 and represent minimum glacial histories with cumulative

386   exposure durations of ~50–125 kyr and cumulative burial durations of ~500–750 kyr. From both

387   transects,^{26}Al/^{10}Be ratios from samples at the ice margin (5.14 ± 0.26; mean ± 1σ) are slightly

388   higher than those from the inland sites (4.47 ± 0.86; excluding the apparent outlier of 2.19 ± 0.16;

389   22GRO-03), though these overlap at 1σ uncertainty.

390

391   *4.3 Constraints on Quaternary ice cover history and erosion*

392   We modeled cosmogenic-nuclide accumulation through the Quaternary to determine whether the

393   measured ^{10}Be and ^{26}Al concentrations across Inglefield Land can be explained by a common

394   exposure history and differential erosion. We tested exposure histories derived from δ^{18}O

395   thresholds between 3.6 and 4.0‰, corresponding to 0.7–1.9 Myr of cumulative exposure and 0.8–

396   2 Myr of cumulative burial over the last 2.7 Myr (Fig. 10). For each of these exposure histories,

397   modeled nuclide concentrations yielded a good fit to those we measured for at least one sample.

398   Yet only the exposure history constructed with a δ^{18}O threshold value of 3.74‰ yields ^{10}Be and

399 ^{26}Al concentrations with a good fit to the data in all bedrock samples except those with ^{26}Al/^{10}Be

400 ratios above the production ratio (22GRO-01 and 22GRD-CR04-SURF), the sample previously

401 identified as an outlier based on its low ^{26}Al/^{10}Be ratio (22GRO-03), and our boulder sample

402 (22GRO-32). However, other scenarios with similar δ^{18}O threshold values of 3.72 and 3.76‰ fit

403 most of the non-outlier bedrock samples, though fewer than our best-fit δ^{18}O threshold value of

404 3.74‰. This best-fitting exposure history corresponds to ~0.9 Myr of total exposure and ~1.8 Myr

405 of total burial over the last 2.7 Myr (Fig. 11). Given this ice-cover scenario, we find model-data

406 agreement with subglacial and subaerial erosion rates ranging between 0 and ~2 x 10^{-3} mm yr^{-1} and

407 0 and ~2 x 10^{-2} mm yr^{-1}, respectively (Fig. 12). For our best-fit exposure scenario using a δ^{18}O

408 threshold values of 3.74, we were not able to simulate erosion rates for bedrock samples that did

409 not have a good fit with this δ^{18}O threshold value (22GRO-01, 22GRO-03, 22GRD-CR04-SURF,

410 and 22GRO-32). While there were some exposure and erosion combinations that were compatible

411 with measurements from our single boulder sample (22GRO-32), we prioritized bedrock samples

412 in assessing whether all sites could have a common Quaternary ice-cover history, as the boulder

413 likely has a different exposure and erosion history than the collocated bedrock. We do not observe

414 clear trends in the modeled subaerial erosion rates, though it we note that subglacial erosion rates

415 are modeled to be greater than about 1 x 10^{-4} mm yr^{-1} for ice margin areas, while these exhibit

416 larger variability for inland and coastal samples.

417

418 **5 Discussion**

419 ***5.1 Differential erosion, ice streams, and ancient landscapes across Inglefield Land***

420 We identified an ancient landscape with our oldest sites retaining at least a ~1.5 Myr history.

421 However, the nuclide concentrations vary throughout the landscape despite the fact that the long-

422   term ice-margin history should be similar across sites, as evidenced by recent retreat and advance

423   (Søndergaard et al., 2020). After the LGM, the ice sheet retreated over Inglefield Land from its

424   maximum extent in Kane Basin. The modern coast deglaciated ~8.5 ka, and ice retreated behind

425   the present margin by 6.7 ka (Søndergaard et al., 2020) corresponding to our entire <50 km

426   transects becoming ice free within 2 kyr. We speculate that the LGM advance across Inglefield

427   Land was likely similarly swift given our field area represents a short distance with respect to the

428   entire ice flowline out to the Greenland Ice Sheet LGM terminus in northern Baffin Bay. These

429   findings suggest that – within error of our ^{26}Al/^{10}Be-derived exposure scenarios – all our sites have

430   experienced similar periods of ice cover and ice-free conditions on glacial-interglacial timescales.

431   This thus begs the question: why do amounts of nuclide inheritance and ^{26}Al/^{10}Be ratios at our

432   coastal, inland, and ice-margin sites differ?

433   Our combined mapping of bedrock lithology, landscape-scale fractures, and lake density

434   as evidence for past glacial erosion, along with field observations of bedrock surface weathering

435   provide a first hint that erosion is responsible for differing ^{26}Al and ^{10}Be concentrations. Though

436   some of the cap rock removal likely occurred before the Quaternary (e.g., Krabbendam and

437   Bradwell, 2014), our mapping of fractures and lakes reveals a clear imprint of differential erosion

438   by the ice sheet. Regions of crystalline bedrock and high lake density inland (with the exception

439   of the areas fronting Hiawatha Glacier) and near the ice margin exhibit weathered bedrock

440   surfaces, diagnostic of cold-based ice cover during the last glacial cycle. Overlapping areas of

441   crystalline bedrock, fractures, and high lake densities in the four valleys leading into Force,

442   Rensselaer, and Dallas bays and in front of Hiawatha Glacier, however, contain fresh, unweathered

443   bedrock outcrops with primary surface features intact. The prevalence of erosion indicators in

444   these areas suggests the presence of erosive ice here with higher velocities than experienced by the

445   surrounding landscape for at least a portion of the last glacial cycle. We posit that these areas were

446   ice stream onset zones during the last glacial cycle and likely earlier glacial cycles as well.

447   The $^{26}Al/^{10}Be$ ratios and lower levels of cosmogenic nuclide inheritance support more

448   erosion at the coastal sites versus the inland and ice margin areas. The samples at 100 m asl in

449   Rensselaer and Marshall valleys have the youngest apparent exposure ages and $^{26}Al/^{10}Be$ ratios

450   close to the production ratio, suggesting removal of the longer burial signal preserved at the upland

451   sites via erosion. Furthermore, the 255 m asl coastal site in Rensselaer Valley has more inheritance

452   and lower $^{26}Al/^{10}Be$ ratios compared to the 100 m asl elevation site, which may reflect differential

453   erosion by an ice stream in the Rensselaer Valley as it increased velocity and erosion down flow.

454   Previous studies on Baffin Island and in Scandinavia used mapping and cosmogenic nuclide

455   measurements to identify areas as ice stream onset zones (Andersen et al., 2018; Briner et al., 2006;

456   Briner et al., 2008; Brook et al., 1996). Ice at these onset zones transitioned from cold-based to

457   warm-based ice and did not erode >3 m during the last glacial cycle, though it is thought that

458   velocities increased downstream from these areas. We find similar cosmogenic nuclide evidence

459   of ice stream onset zones at the mouths of Rensselaer and Marshall bays, suggesting that ice

460   streams may have initiated in these areas during glacial maxima.

461   Cosmogenic nuclide concentrations in weathered bedrock surfaces at our inland and ice

462   margin sites retain combined minimum exposure and burial signals of 500 kyr to 1500 kyr,

463   demonstrating the antiquity of the landscape across Inglefield Land. The preservation of these

464   inland and ice margin landscapes implies past cold-based ice conditions and, in turn, low erosion

465   across Inglefield Land through multiple glacial cycles. This also suggests the erosional landscapes

466   seen in mapping across the interior of Inglefield Land (i.e., lack of cap rocks and exposed

467   crystalline basement, high lake densities, and bedrock fractures) were created prior to the last

468   glaciation.

469   Such old, low-erosion landscapes have been preserved in other glaciated parts of the Arctic.

470   Our results are similar to studies from southern, western, northwestern, and northeastern Greenland

471   and Baffin Island that identify long-preserved (often > 1000 kyr), ancient landscapes with low

472   amounts of erosion and high amounts of cosmogenic nuclide inheritance (Andersen et al., 2020;

473   Beel et al., 2016; Bierman et al., 1999; Briner et al., 2006; Ceperley et al., 2020; Corbett et al.,

474   2016a; Miller et al., 2006; Roberts et al., 2013; Sbarra et al., 2022; Skov et al., 2020; Søndergaard

475   et al., 2020). Similarly, the pattern of significantly lower cosmogenic nuclide inventories at lower,

476   coastal areas in less preserved landscapes is seen elsewhere in Greenland and the Canadian Arctic.

477   In eastern Greenland, for example, Skov et al. (2020) found higher degrees of cosmogenic nuclide

478   inheritance in weathered bedrock uplands and lower concentrations in sculpted bedrock closer to

479   the coast around Dove Bugt, attributing this to a polythermal ice sheet with efficient erosion at

480   lower elevations. Studies on Baffin Island using ^{10}Be and ^{26}Al measurements found transitions

481   from cold-based and non-erosive to warm-based and erosive ice at lower elevations near the coast

482   (e.g., Briner et al., 2006; Briner et al., 2008), supporting our conclusions of transitions from cold-

483   based to warm-based ice near the coast of Inglefield Land.

484

485   *5.3 Can measured ^{26}Al/^{10}Be ratio differences be explained with a common ice-cover history and*

486   *variable erosion rates?*

487   We tested our hypothesis that the disparate nuclide concentrations across Inglefield Land could

488   have resulted from a shared Quaternary exposure history and differential erosion. Indeed, we found

489   that the ^{10}Be and ^{26}Al concentrations in most of our bedrock samples can be explained through a

490   Pleistocene ice-cover history with 0.9 Myr cumulative exposure and 1.8 Myr cumulative burial,

491   and sample-varying subglacial and subaerial erosion rates.

492   The range of sub-aerial erosion rates (0–2 x 10^{-2} mm yr^{-1}) that provide good fits to the

493   measured nuclide concentrations for our preferred exposure history are broadly consistent with

494   sub-aerial erosion rates measured in other cold, arid, polar environments. There are no clear

495   patterns of spatial variability across the landscape, though estimates from 22GRO-48 at the coast

496   exhibit the largest range of possible subaerial erosion rates. A global synthesis found mean

497   subaerial erosion rates at rock outcrops are 13 x 10^{-3}, 8 x 10^{-3}, and 4 x 10^{-3} mm yr^{-1} in cold, arid,

498   and polar environments, respectively (Portenga and Bierman 2011). A cosmogenic nuclide-based

499   study from the southern Ellsworth Mountains, Antarctica found longer-term subaerial erosion rates

500   of 5.52 ± 0.26 x 10^{-3} mm yr^{-1} for gneiss (Marrero et al., 2018), similar to those derived from Baffin

501   Island gneiss of 2 x 10^{-3} mm/yr (Margreth et al., 2016). Furthermore, subaerial erosion of gneiss

502   in the polar regions is thought to occur primarily through mineral- and granular-scale processes,

503   including abrasion and disintegration, and are accelerated by wind-blown sediments (Margreth et

504   al., 2016). We noted abundant gruss around our inland and ice-margin sites and near constant

505   winds with wind-transported sediments, suggesting that these processes may be responsible for

506   subaerial erosion in Inglefield Land. Additionally, the presence of weathering features including

507   gruss and weathering pits across Inglefield Land indicate that subaerial erosion likely varies not

508   only from outcrop to outcrop as a result of varying lithology, but also across individual bedrock

509   outcrops (e.g., sampled from near an old weathering pit).

510   Subglacial erosion rates that yield good model-data fits are between 0 and ~2 x 10^{-3} mm

511   yr^{-1} across our sites, and all samples have possible subglacial erosion rates >~1 x 10^{-4} mm yr^{-1}.

512   Samples at the ice margin do not have modeled erosion rates below this value, and their maximum

513   modeled erosion rates (~1 x 10^{-3} mm yr^{-1}) are higher modeled maximum erosion rates at the inland

514   sites (~5 x 10^{-4} mm yr^{-1}). This indicates that the bedrock surfaces at the modern ice margin are

515   consistently eroded during ice burial and may experience higher subglacial erosion rates. Some

516   inland sites have subglacial erosion rates of zero mm yr^{-1}, thus highlighting the potential for spatial

517   variability of subglacial erosion rates under a cold-based ice sheet. Furthermore, subglacial erosion

518   rate estimates from our sites with the lowest levels of cosmogenic nuclide inheritance (at the coast)

519   exhibit the largest spread in modeled subglacial erosion rates. These coastal samples also have

520   wide ranges of subaerial erosion rates, and while lower nuclide concentrations indicates that at

521   either subglacial or subaerial erosion must be high to limit nuclide accumulation, we cannot

522   determine which kind of erosion is more significant.

523   Overall, subglacial erosion rate estimates across Inglefield Land are generally lower than

524   those measured elsewhere in Greenland. Many of these previous estimates, however, come from

525   warm-based glaciers, while our results suggest that Inglefield Land was covered primarily by cold-

526   based ice. The upper range of our modeled sub-glacial erosion rates agree with those from east

527   Greenland derived from sediment flux data of $1 - 4$ x 10^{-2} mm yr^{-1} (Andrews et al., 1994), though

528   this was later updated by Cowton et al. (2012) to 3 x 10^{-1} mm yr^{-1} to account for sediment entrained

529   in icebergs (Syvitski et al., 1996). In central-west Greenland, suspended sediment measurements

530   from the Watson River yielded average subglacial erosion rates of 5 x 10^{-1} mm yr^{-1}, with annual

531   erosion rates as high as 4.5 mm yr^{-1} and 4.8 ± 2.6 mm yr^{-1}, all higher than our modeled rates

532   (Cowton et al., 2012; Hasholt et al., 2018; Hogan et al., 2020). Glaciomarine deposits near

533   Petermann Glacier, northwest Greenland and at the mouth of Jakobshavn Isfjord constrain erosion

534   rates during the last deglaciation to $0.29 - 0.34$ mm yr^{-1} and 0.52 mm yr^{-1}, respectively (Hogan et

535   al., 2012; Hogan et al., 2020). Finally, Balter-Kennedy et al. (2021) determined centennial-scale

536   subglacial erosion rates of $3 - 8 \times 10^{-1}$ mm yr^{-1} and orbital-scale rates of $1 - 3 \times 10^{-1}$ mm yr^{-1} near

537   Jakobshavn Isbræ. These previously derived subglacial erosion rates may be higher than what we

538   report because they come from places with different ice sheet thermal states. Thus, these estimates

539   of subglacial erosion could reflect periods when temperatures were generally warmer or periods

540   of warming, which can lead to higher subglacial erosion rates because of increased basal

541   temperatures and subglacial sliding, perhaps in part due to increased meltwater delivery to the bed

542   in warmer climates (Alley et al., 2019). Additionally, these studies of glacial erosion focus on

543   relatively short timescales (<multi-millennial), while our modeled erosion rates are integrated over

544   the Quaternary, perhaps highlighting the effects of temporal integration as previously noted by

545   Koppes and Montgomery (2009) and Spotila et al. (2004).

546   Cold-bedded glaciers are commonly considered non-erosive, yet glacial erosional features

547   (striae, scrapes, grooves, and isolated blocks) in landscapes otherwise protected by cold-based ice

548   demonstrate their erosional capacity (Atkins et al., 2002; Cuffey et al., 2000; Sugden, 1978;

549   Sugden et al., 2005; Ugelvig and Egholm, 2018). Our modeled sub-glacial erosion rates between

550   0 and ~2×10^{-2} mm yr^{-1} in mapped areas of cold-based ice cover point to the erosive nature of cold-

551   based glaciers and are consistent with previous estimates of erosion. Syntheses found modern sub-

552   glacial erosion rates under frozen-bedded glaciers on the Antarctic Peninsula to be between 1×10^{-2}

553   and 1×10^{-1} mm yr^{-1} (Koppes et al., 2015), while on the Meserve Glacier, a cold-based alpine

554   glacier in Victoria Land, Antarctica, subglacial erosion rates have been estimated to be 2×10^{-3}

555   mm yr^{-1} (Cuffey et al., 2000). Studies of tors in the Cairngorm Mountains, Scotland, yield

556   subglacial erosion estimates of ~4.4×10^{-3} mm yr^{-1} during cover by a cold-based Celtic Ice Sheet

557   (Phillips et al., 2006). Various mechanisms have been proposed for erosion by cold-bedded

558   glaciers. Frozen bedded glaciers entrain debris at their bed and can minorly abrade and pluck

559   bedrock surfaces (Atkins et al., 2002; Cuffey et al., 2000; Sugden, 1978; Sugden et al., 2005;

560   Ugelvig and Egholm, 2018). Extensive studies from the Cairngorm Mountains in Scotland using

561   cosmogenic nuclides and geomorphic models of tor formation and erosion found cold-based ice

562   erosion was potentially capable of significantly modifying pre-existing landforms (Goodfellow et

563   al., 2014; Hall and Glasser, 2003; Hall and Phillips, 2006; Phillips et al., 2006).

564   In sum, we find that the disparate nuclide concentrations across Inglefield Land can be

565   explained by a common Quaternary exposure/burial history if erosion rates are allowed to vary

566   sample-by-sample. Erosion rates consistent with the cosmogenic data are similar with previously-

567   published estimates in polar areas covered by cold-based glaciers. Variability in erosion rates

568   across the landscape likely reflect differences in lithology, as well as subglacial conditions. By

569   allowing our erosion rates to vary at each sampling location, in our model, we are able to account

570   for potential erosional variability resulting from local differences in lithology (e.g., mineralogy

571   and crystal size) landscape position, and sampling location (e.g., within an old weathering pit or a

572   zone of high grussification). However, our model does not account for temporal variability in sub-

573   glacial erosion. Temporal variability (abrasion versus quarrying) should be diminished when

574   averaged across many glacial cycles, but the imprint of variable glacial erosion during the last

575   glacial cycle (e.g., a site of cobble-sized block of bedrock removed beneath mostly frozen ice;

576   Atkins et al., 2002; Hall and Phillips, 2006) may lead to differences in the resulting sub-glacial

577   erosion rates. Furthermore, the basal zone across Inglefield Land may have transitioned from less-

578   erosive to more-erosive and back to less-erosive during switches between warm- and cold-bedded

579   conditions through the thickening and thinning of the ice sheet during a glacial cycle. This could

580   lead to time-varying sub-glacial erosion rates and shorter periods of increased glacial erosion, as

581   evidenced by the glacial sculpting at our coastal sites.

582   *5.4 Long-term ice sheet fluctuations across Inglefield Land*

583   ^{26}Al/^{10}Be ratios from our oldest bedrock surfaces suggest that, at a minimum, the Greenland Ice

584   Sheet covered Inglefield Land for 1200 kyr and was smaller than today for 400 kyr over the last

585   1600 kyr. We determined that a Quaternary exposure history with ~0.9 Myr of cumulative

586   exposure and ~1.8 Myr of cumulative burial (constructed using our best-fit δ^{18}O threshold of

587   3.74‰) is consistent with the measured cosmogenic-nuclide concentrations in nearly all of our

588   bedrock surfaces when erosion rates are allowed to vary for each sample. In this preferred exposure

589   scenario, much of the exposure takes place between 2.7 and 1.2 Ma before the mid-Pleistocene

590   transition, but still requires ice-free conditions (and exposure) within the last ~1.2 Myr during

591   major interglacials.. These periods of exposure are of particular interest as they indicate times

592   when the Greenland Ice Sheet was at its present extent or smaller.

593   Our results complement limited other terrestrial studies of Greenland Ice Sheet stability

594   throughout the Quaternary. ^{26}Al/^{10}Be measurements from the GISP2 bedrock core from under the

595   center of the Greenland Ice Sheet revealed that the ice sheet was present for most of the Quaternary

596   but was nearly completely absent at least once in the last 1.1 Myr (Schaefer et al., 2016). Studies

597   of basal material from Camp Century show similar results, indicating that the northwestern

598   Greenland Ice Sheet was present through most of the Pleistocene (Christ et al., 2021). Additionally,

599   when compared to studies these of material from under the modern Greenland Ice Sheet, our results

600   suggest that Inglefield Land was ice-free throughout much more of the Quaternary than interior

601   sectors (i.e., currently covered by the modern ice sheet), logical given that Inglefield Land would

602   be completely covered only during glacial maxima. When taken at face-value, our preferred

603   exposure history corresponding to a δ^{18}O threshold of 3.74‰ indicates that the northwestern

604   Greenland Ice Sheet persisted at an extent larger-than-today throughout some Pleistocene

605 interglacials, further supported by similar findings from the Laurentide Ice Sheet (Leblanc et al.,

606 2023).

607

608 **6 Conclusions**

609 ● Geologic mapping partitions Inglefield Land into zones of glacial erosion and protection

610 revealing restricted zones of erosion in lower Force, Rensselaer, and Marshall valleys and

611 in front of Hiawatha Glacier as ice-velocity increased coastward into ice streams;

612 elsewhere landscapes were likely covered by low erosion (e.g., frozen-bedded) regimes.

613 ● Patterns of glacial erosion are confirmed with cosmogenic nuclide measurements,

614 revealing an ancient landscape across Inglefield Land. This implies widespread cold-based

615 ice cover across much of Inglefield Land during Quaternary glacial cycles, even during

616 transitions between interglacial and glacial periods. These measurements also indicate that,

617 despite cosmogenic nuclide inheritance, there was perhaps temporarily warm-based ice at

618 coastal sites during the last glacial cycle when the Greenland Ice Sheet extended well

619 beyond Inglefield Land, and ice streams originated near the mouths of the modern Force,

620 Rensselaer, and Marshall bays. Mapping and cosmogenic nuclide measurements allow us

621 to differentiate between areas of cold- and warm-based ice offering a clear look into the

622 polythermal nature of former ice sheets.

623 ● Differential subglacial and subaerial erosion explains disparate cosmogenic nuclide

624 concentrations found at our inland and ice margin sites. Modeled subaerial erosion rates

625 match those found in other polar regions for similar lithologies. Our modeled subglacial

626 erosion rates are lower than those previously calculated for Greenland, as other studies

627   focused on warm-based parts of the Greenland Ice Sheet. We provide estimates of

628   subglacial erosion under cold-bedded conditions.

629   ● Ice cover durations derived from $^{26}Al/^{10}Be$ ratios and cosmogenic nuclide modeling reveal

630   a common ice sheet history, and variable erosion rates indicate that the ice sheet

631   persistently covered Inglefield Land for approximately one-third of the last 2.7 Myr. This

632   exposure occurred mostly early in the Quaternary before the mid-Pleistocene transition.

633   Like other findings (e.g., LeBlanc et al., 2023), when taken at face value, our $\delta^{18}O$ threshold

634   value when applied to the global $\delta^{18}O$ stack implies ice-cover during some middle and late

635   Pleistocene interglacials. Our results also suggest that the Greenland Ice Sheet was at its

636   current extent or smaller during several interglacial periods, adding to the body of literature

637   that indicate a dynamic Greenland Ice Sheet throughout the Quaternary.

638   ● Bedrock surfaces across much of Inglefield Land were not greatly eroded during the LGM

639   and contain a long-term cosmogenic nuclide memory of ice sheet fluctuations through the

640   mid-Pleistocene – at a minimum. Our bedrock sampling strategy and measurements

641   provide an analog for information contained in sub-ice material under the Greenland Ice

642   Sheet, indicating that this material should contain valuable cosmogenic nuclide archives of

643   ice sheet change during minimum phases.

644

645

646

647

648

649

650 **Code availability**

651 All MATLAB codes and data used in the study are provided in the supplementary materials.

652

653 **Data availability**

654 All cosmogenic nuclide data required to calculate exposure ages are included in the supplementary

655 materials.

656

657 **Financial support**

658 CKW and JPB were supported by NSF grant #1933938 and ABK, JMS, and NEY were supported

659 by NSF grant #1933927.

660

661 **Author contributions**

662 All authors designed the study and conducted fieldwork. CKW undertook GIS mapping and lab

663 work. ABK led modeling of cosmogenic nuclide results. CKW, JPB, and ABK wrote the first draft

664 of the manuscript and created all figures. All authors edited and contributed to subsequent

665 manuscript drafts.

666

667 **Competing interests**

668 The authors declare that they have no conflict of interest.

669

670 **Acknowledgements**

671 Inglefield Land is part of the lands traditionally inhabited by the Inughuit. We thank the people

672 and government of Greenland for allowing us to conduct fieldwork on the island, service people

673   and workers at Pittufik Space Base for their hospitality, Kyli Cosper at Polar Field Services for

674   logistical support, Air Greenland for helicopter flights, Karlee Prince, Red Stein, Brandon Graham,

675   and Jen Smola for help in the field, and Roseanne Schwartz and Maya Lasker for lab assistance.

676

677

678

679

680

681

682

683

684

685

686

687

688

689

690

691

692

693

694

695

696 **Figures**

697

698
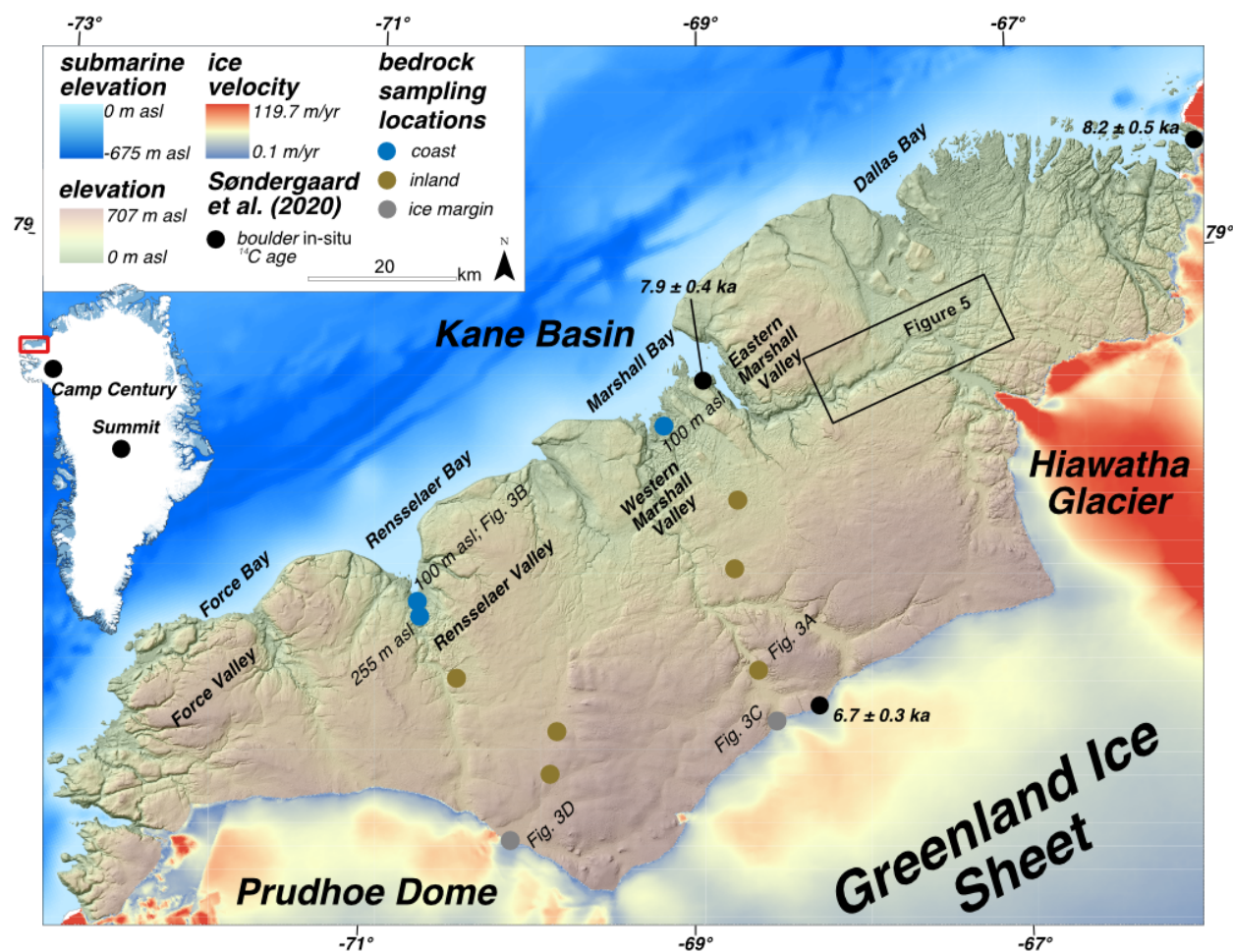
699 *Figure 1: Overview map of Inglefield Land and key geographic locations. Ice velocity from Joughin et al. (2018); 25*
700 *m DEM from Korsgaard et al. (2016).*

701

702

703

704

705

706

707

708

709

710

711
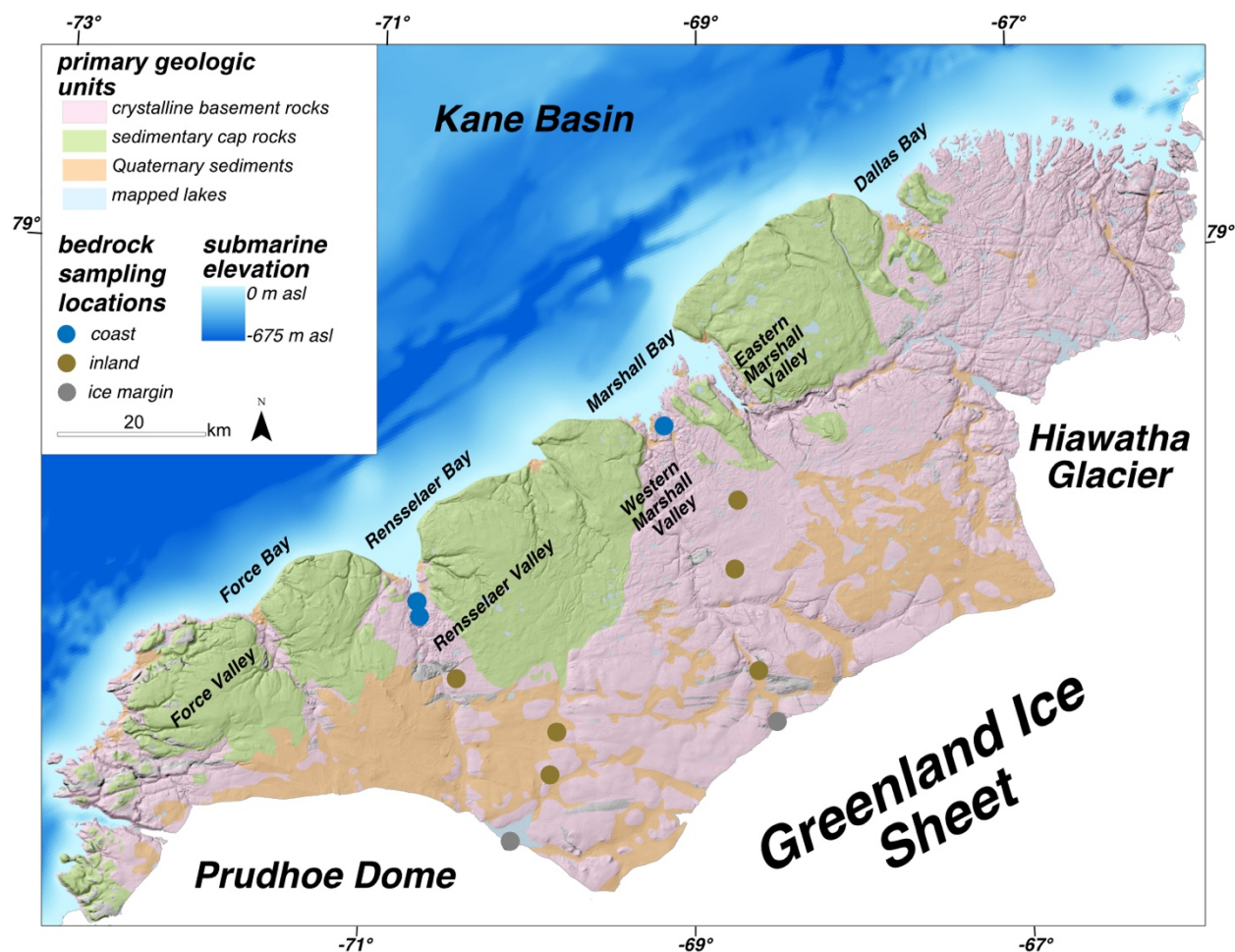
Figure 2: simplified geologic map of Inglefield Land (Kokfelt et al., 2023).

714

715

716

717

718

719

720

721

722

723

724
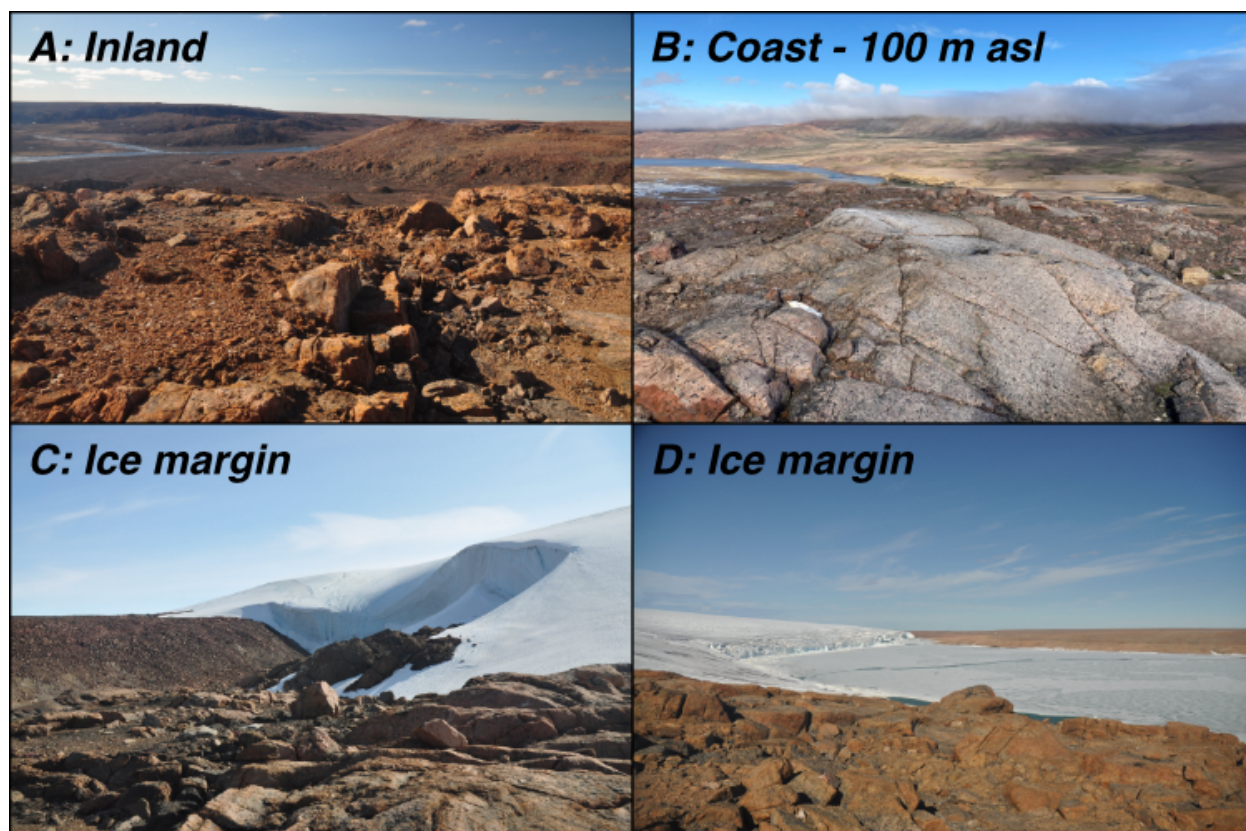
725

726

727 *Figure 3: representative images of bedrock surfaces at sample sites in Inglefield Land. Photo locations show on Fig.*
728 *1. .*

729

730

731

732

733

734

735

736

737

738

739

740

741

742

743
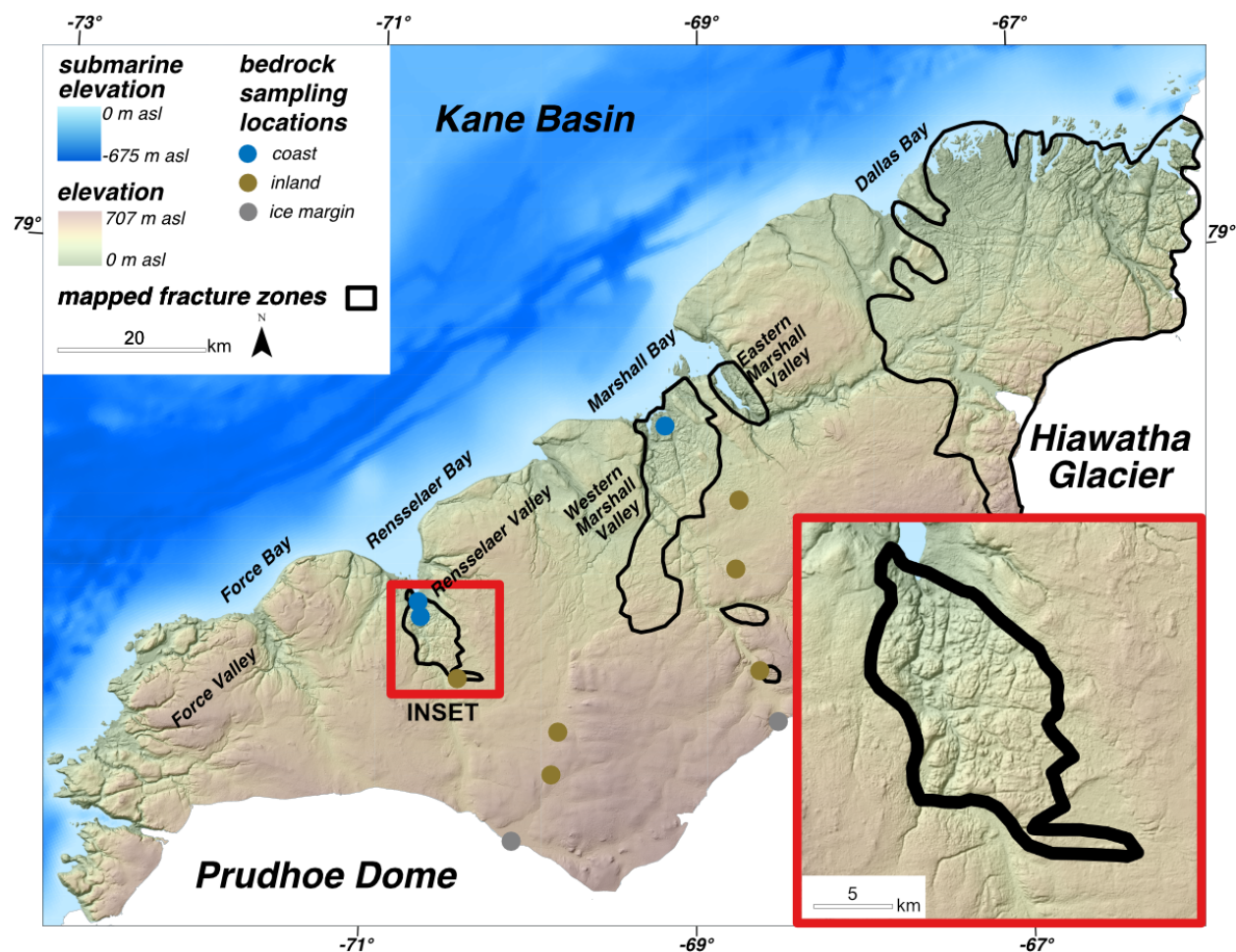
744 *Figure 4: mapped fracture zones in Inglefield Land. Inset shows zoom-in of fracture zone in Rensselaer Valley.*

745

746

747

748

749

750

751

752

753

754
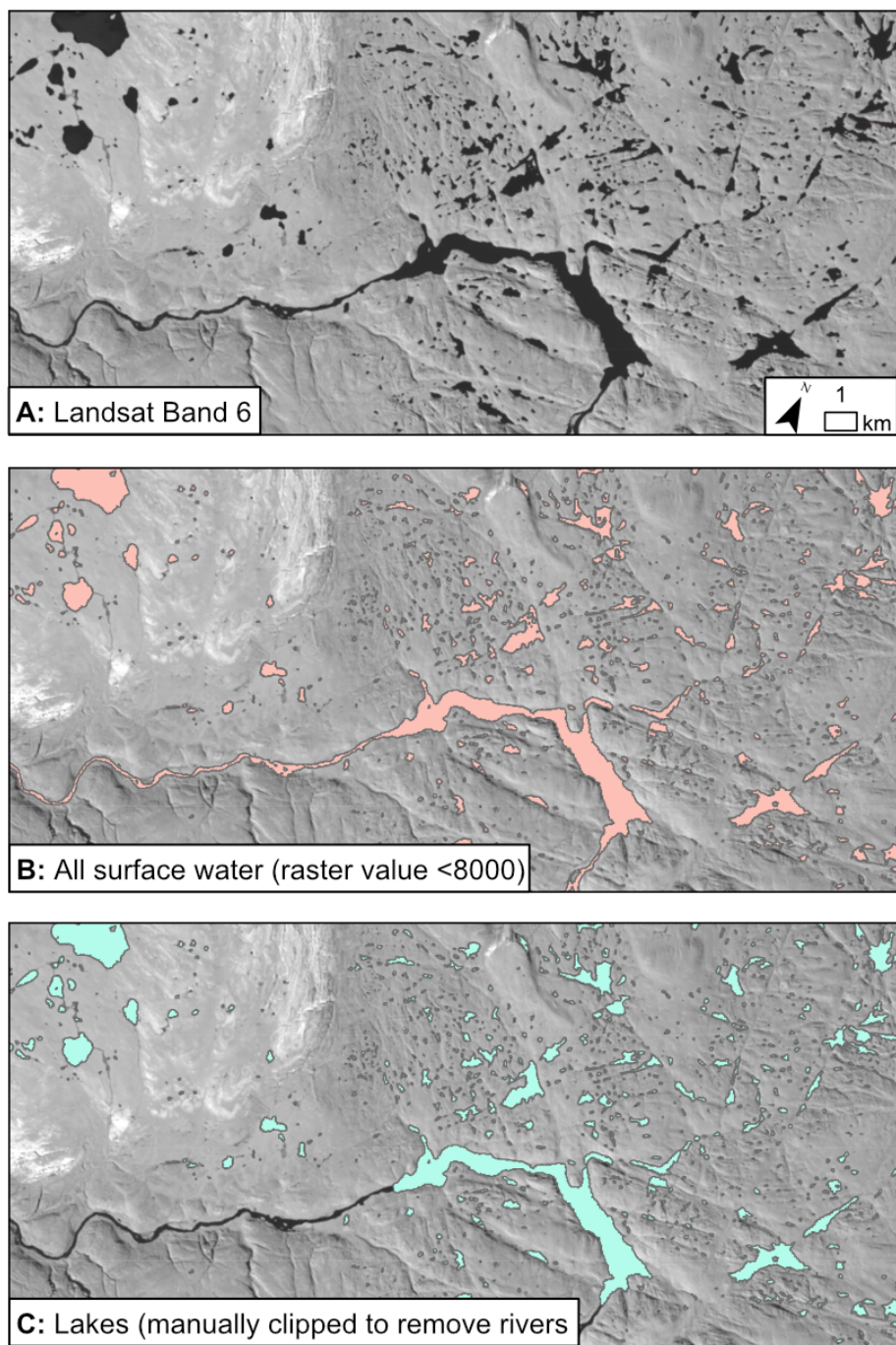
755

756   *Figure 5: LANDSAT Band 6 image (A) of portion of Inglefield Land shown inf Fig. 1, showing workflow of*
757   *automatically selecting surface water (B) with a threshold value of 8000 and manually removing rivers (C).*

758

759

760

761

762

763
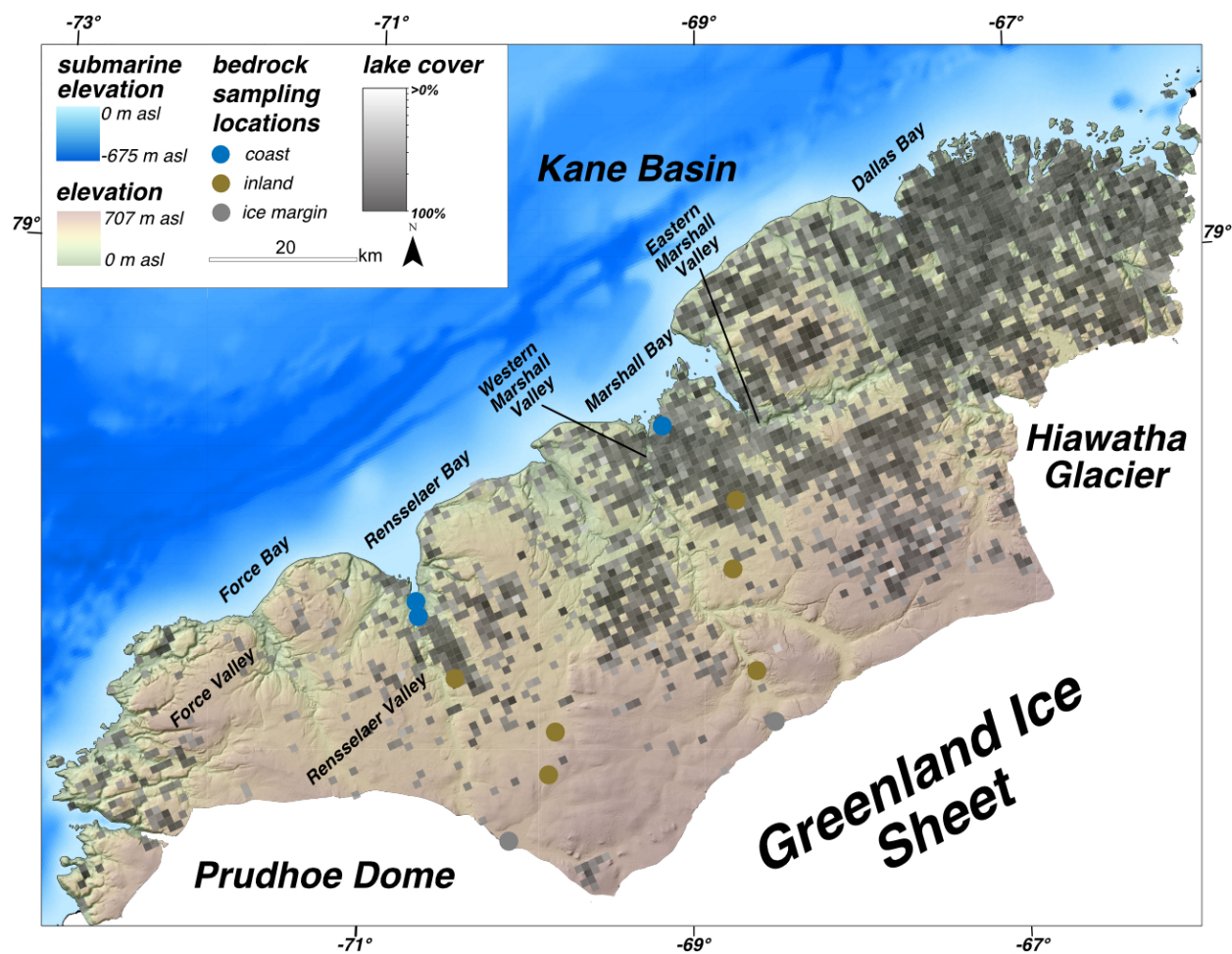
Figure 6: map of lake densities across Inglefield Land. Grid cells are 1 km².

765

766

767

768

769

770

771

772

773

774

775

776

777

778
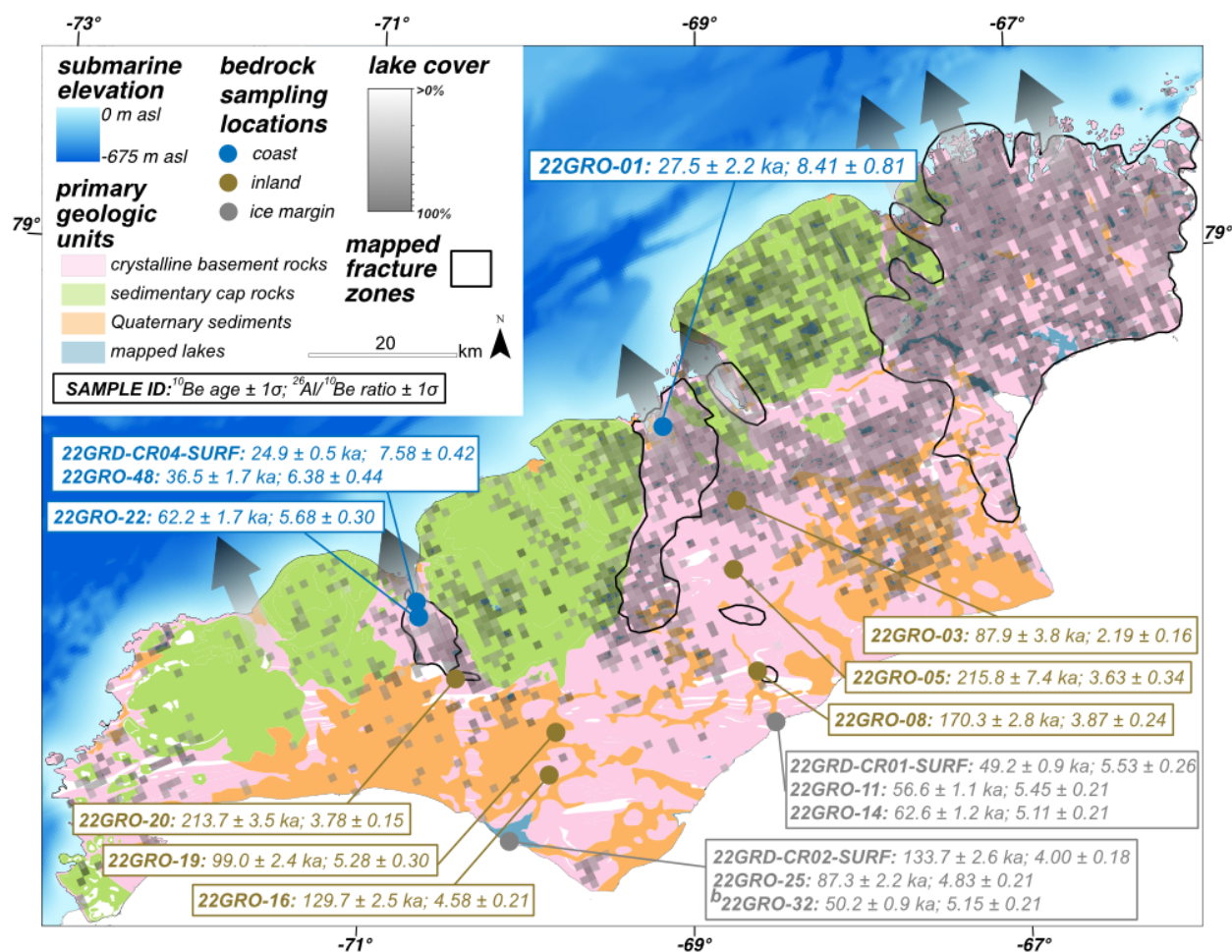
Figure 7: combined map of bedrock lithology, fracture zones, and lake densities with cosmogenic nuclide results. Semi-transparent arrows show zones of increased erosion as indicated by mapping proxies; arrow size does not correspond to amount of erosion, rather they just mark the areas of erosion.. [b]Boulder sample

783

784

785

Figure 8: subset of bedrock sample photos and resultant cosmogenic nuclide results. Note the smoothness of the coastal outcrops compared to the rough, weathered textures of the inland and ice-margin sites.

793

794

795

796

797

798

799
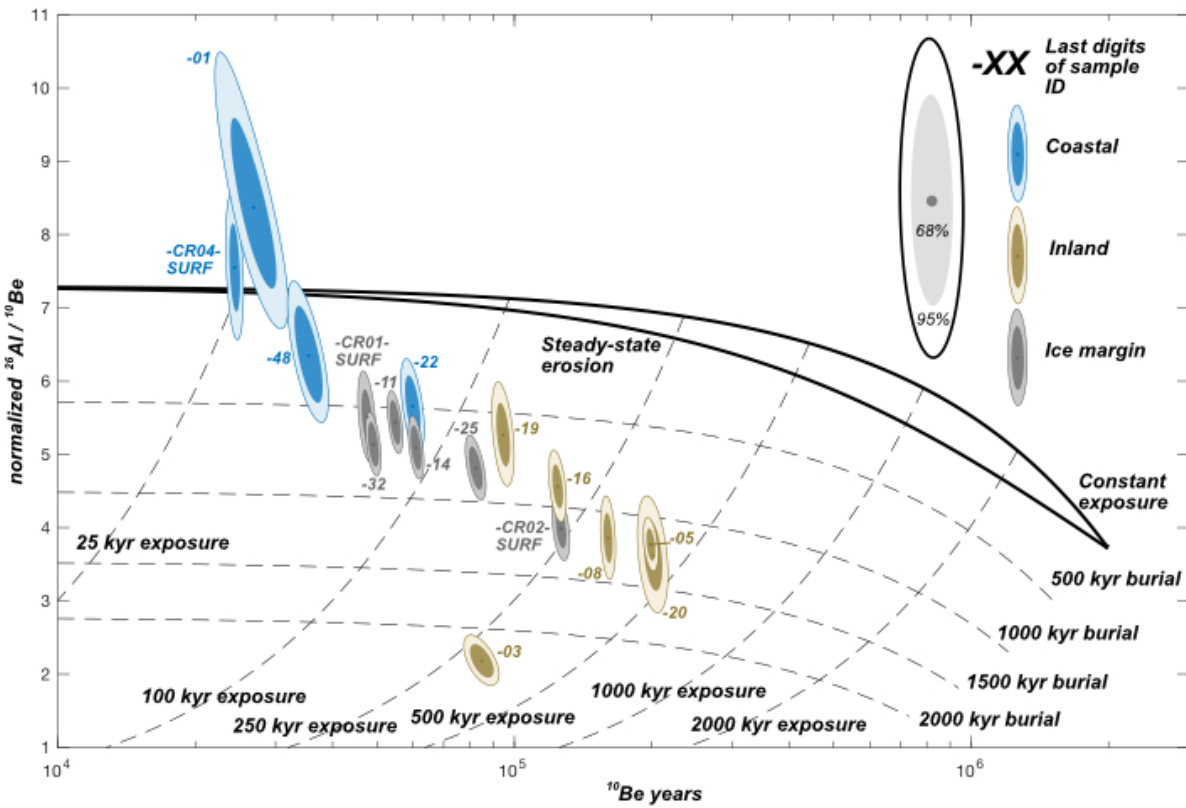
Figure 9: $^{26}Al/^{10}Be$ two-nuclide diagram. Concentrations normalized to Arctic high latitude, sea level ^{10}Be production rate of 3.96 atoms g yr^{-1} using Greenland-specific $^{26}Al/^{10}Be$ surface production ratio of 7.3 (Corbett et al., 2016; Young et al., 2013).

804

805

806

807

808

809

810

811

812

813
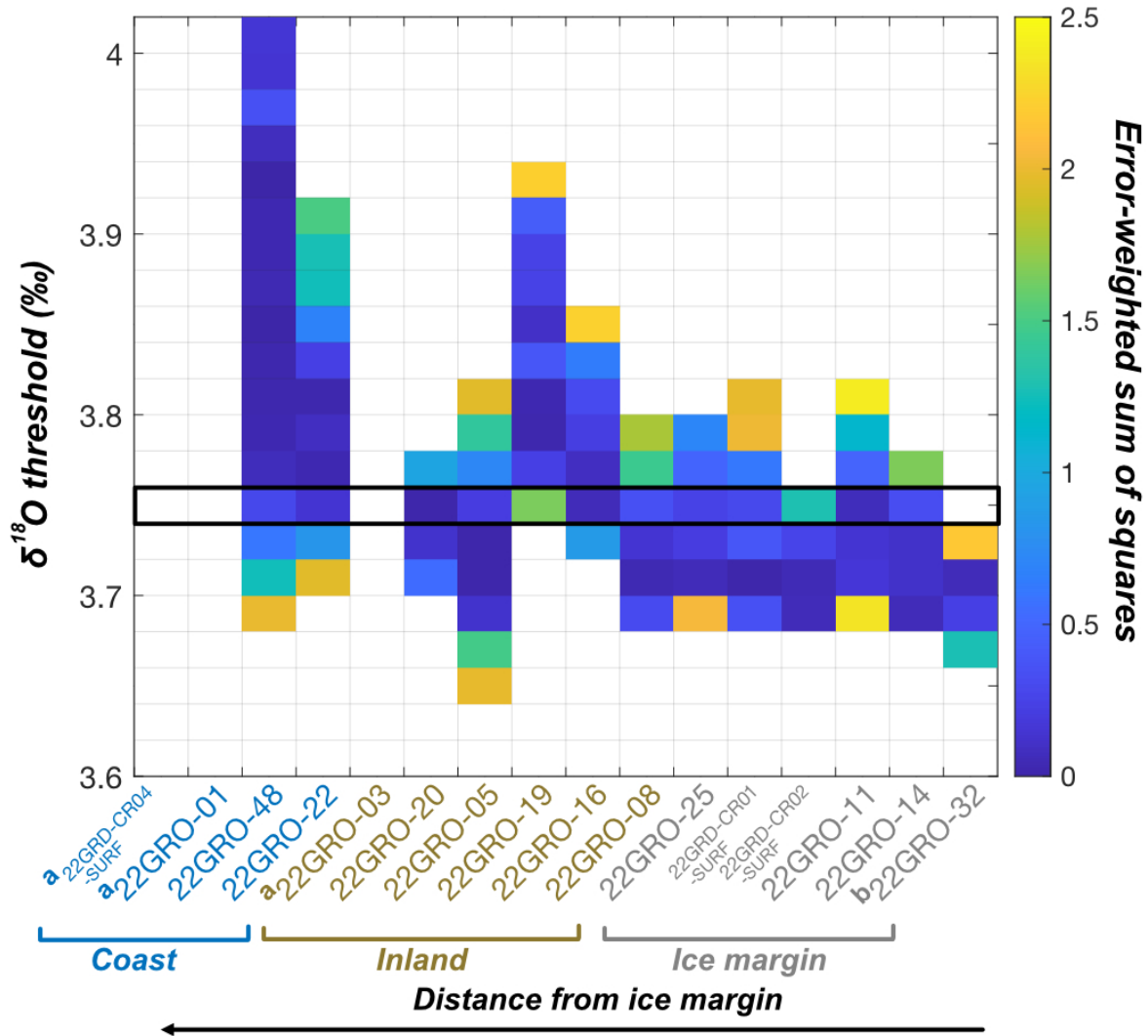
Figure 10: Model-data fits for exposure histories constructed with δ¹⁸O thresholds of 3.60-4.00‰. For each δ¹⁸O threshold, we modeled cosmogenic nuclide concentrations for each sample using subaerial and subglacial erosion rates ranging from 0 to 2.5 x 10⁻¹ mm yr⁻¹ mm/yr. Colored tiles show the best/lowest error-weighted sums of squares (EWSS) for each sample and δ¹⁸O threshold across all tested erosion rate combinations. We consider an EWSS <2.5 to be an acceptable model-data fit. White tiles indicate that no combination of erosion rates yielded an EWSS <2.5. An exposure history constructed with a δ¹⁸O threshold of 3.74‰, outlined in black box, was the only exposure history we tested that gave an acceptable fit for all non-outlier bedrock samples. ᵃoutlier samples identified with ²⁶Al/¹⁰Be ratios. ᵇboulder sample.

822

823

824

825

826

827
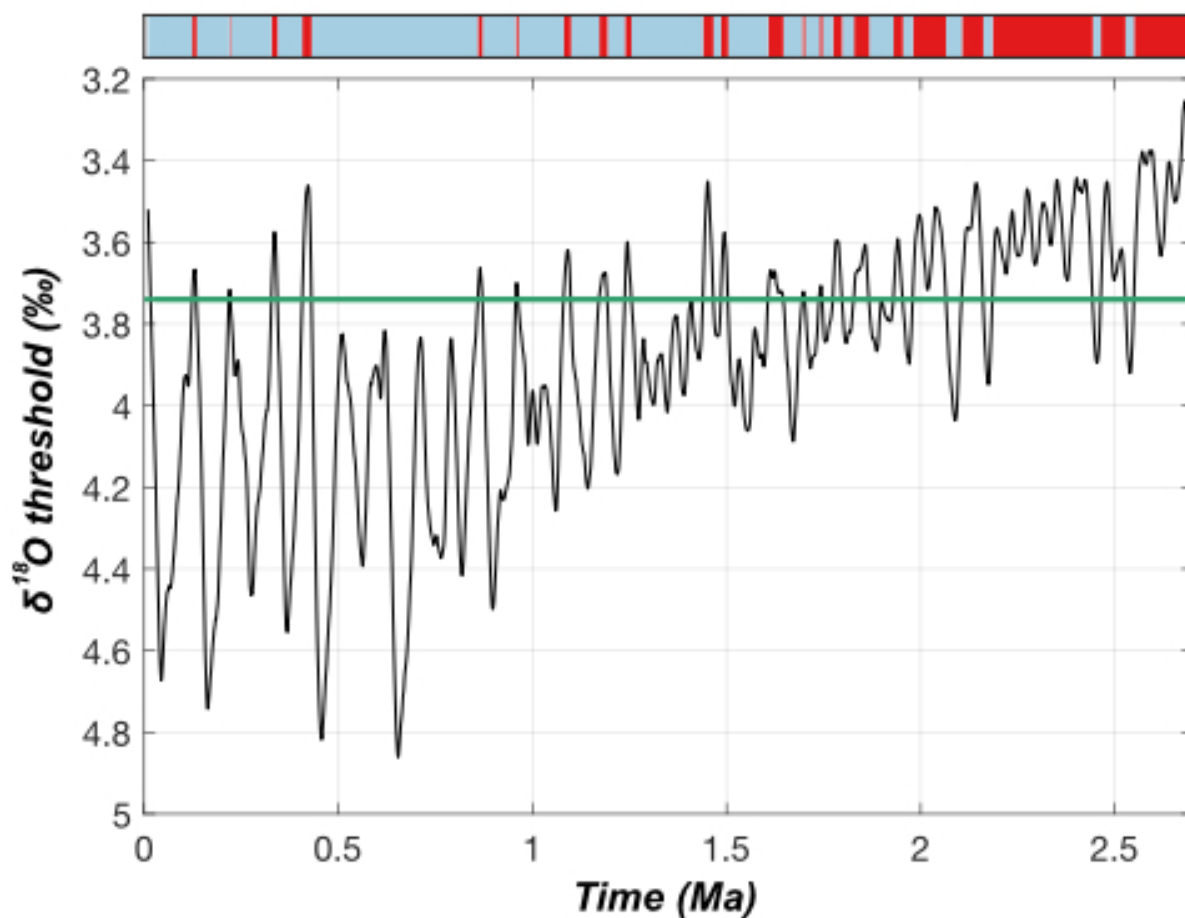
Figure 11: Exposure history constructed with a 3.74‰ δ¹⁸O threshold (teal line) on the LR04 stack (Lisiecki and Raymo, 2005), below which we considered the site ice-free and above which we considered the site ice-covered. The resulting exposure history is shown in the top panel, where periods of exposure are red, and periods of burial are blue. This is the only exposure history we tested that, even when considering site-specific subaerial and subglacial erosion rates, yielded an acceptable fit for all non-outlier bedrock samples. Note Holocene exposure is decoupled from the δ¹⁸O threshold-based exposure duration calculations and is thus not represented on the plot.

834

835

836

837
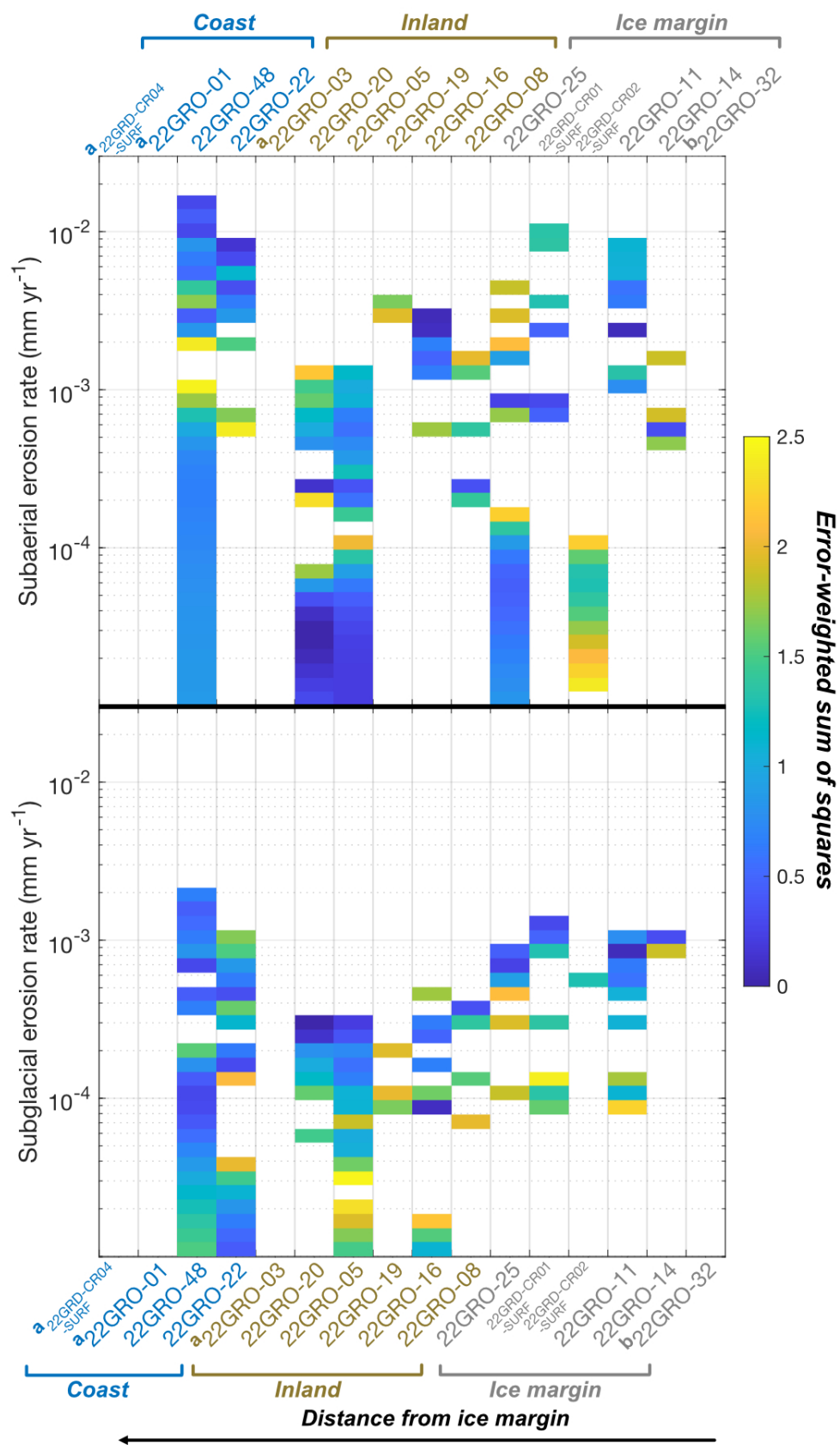
839 *Figure 12: Model-data fits for tested subaerial (top) and subglacial (bottom) erosion rates for our preferred exposure*
840 *history constructed with a $\delta^{18}O$ threshold of 3.74‰. Colored tiles show the best/lowest error-weighted sums of squares*
841 *for tested erosion rate for each sample. White tiles indicate that, for this exposure history, there is no combination of*
842 *subaerial and subglacial erosion that yield a good fit to the data. For example, in combination with subaerial erosion,*
843 *only one tested subglacial erosion rate (5 x 10^{-4} mm yr^{-1}) yielded an acceptable fit for sample 22GRD-CR02-SURF.*
844 *Yet, when applying that subglacial erosion rate, subaerial erosion rates ranging from 0.2–1.2 x 10^{-4} mm yr^{-1} yielded*
845 *an acceptable model-data fit. We tested subaerial and subglacial erosion rates from 0 to 2.5 x 10^{-1} mm yr^{-1}. For no*
846 *sample was there an acceptable model-data fit for the preferred exposure history when either erosion rate was >2.5*
847 *x 10^{-2} mm yr^{-1}. In addition, any sample that yielded a good model-data fit for an erosion rate of 1 x 10^{-5} mm yr^{-1}, we*
848 *also found good fits down to 0 mm yr^{-1} (no erosion of that type). For clarity, the y-axis for both panels is restricted to*
849 *1 x 10^{-5} to 2.5 x 10^{-2} mm yr^{-1}. [a]outliers identified from $^{26}Al/^{10}Be$ ratios. [b]boulder sample.*

850

851

852

853

854

855

856

857

858

859

860

861

862

863

864

865

866

867

868

869 **References**

870 Alley, R. B., Cuffey, K. M., and Zoet, L. K.: Glacial erosion: status and outlook, Annals of
871   Glaciology, 60, 1-13, 10.1017/aog.2019.38, 2019.
872 Andersen, J. L., Egholm, D. L., Olsen, J., Larsen, N. K., and Knudsen, M. F.: Topographical
873   evolution and glaciation history of South Greenland constrained by paired 26Al/10Be
874   nuclides, Earth and Planetary Science Letters, 542, 116300,
875   https://doi.org/10.1016/j.epsl.2020.116300, 2020.
876 Andersen, J. L., Egholm, D. L., Knudsen, M. F., Linge, H., Jansen, J. D., Pedersen, V. K., Nielsen,
877   S. B., Tikhomirov, D., Olsen, J., and Fabel, D.: Widespread erosion on high plateaus during
878   recent glaciations in Scandinavia, Nature Communications, 9, 830,
879   https://doi.org/10.1038/s41467-018-03280-2, 2018.
880 Andrews, J. T., Clark, P. U., and Stravers, J. A.: The patterns of glacial erosion across the eastern
881   Canadian Arctic, Quaternary environments: Eastern Canadian Arctic, Baffin Bay, and
882   West Greenland. Edited by JT Andrews. Allen and Unwin, Winchester, Massachusetts, 69-
883   92, 1985.
884 Andrews, J. T., Milliman, J. D., Jennings, A. E., Rynes, N., and Dwyer, J.: Sediment Thicknesses
885   and Holocene Glacial Marine Sedimentation Rates in Three East Greenland Fjords (ca.
886   68°N), The Journal of Geology, 102, 669-683, 10.1086/629711, 1994.
887 Aschwanden, A. and Brinkerhoff, D. J.: Calibrated mass loss predictions for the Greenland Ice
888   Sheet, Geophysical Research Letters, n/a, e2022GL099058,
889   https://doi.org/10.1029/2022GL099058, 2022.
890 Atkins, C. B., Barrett, P. J., and Hicock, S. R.: Cold glaciers erode and deposit: Evidence from
891   Allan Hills, Antarctica, Geology, 30, 659-662, 10.1130/0091-
892   7613(2002)030<0659:CGEADE>2.0.CO;2, 2002.
893 Balco, G.: Production rate calculations for cosmic-ray-muon-produced 10Be and 26Al
894   benchmarked against geological calibration data, Quaternary Geochronology, 39, 150-173,
895   https://doi.org/10.1016/j.quageo.2017.02.001, 2017.
896 Balco, G., Stone, J. O., Lifton, N. A., and Dunai, T. J.: A complete and easily accessible means of
897   calculating surface exposure ages or erosion rates from 10Be and 26Al measurements,
898   Quaternary Geochronology, 3, 174-195, https://doi.org/10.1016/j.quageo.2007.12.001,
899   2008.
900 Balco, G., Brown, N., Nichols, K., Venturelli, R. A., Adams, J., Braddock, S., Campbell, S.,
901   Goehring, B., Johnson, J. S., and Rood, D. H.: Reversible ice sheet thinning in the
902   Amundsen Sea Embayment during the Late Holocene, The Cryosphere, 17, 1787-1801,
903   https://doi.org/10.5194/tc-17-1787-2023, 2023.
904 Balter-Kennedy, A., Young, N. E., Briner, J. P., Graham, B. L., and Schaefer, J. M.: Centennial-
905   and Orbital-Scale Erosion Beneath the Greenland Ice Sheet Near Jakobshavn Isbræ,
906   Journal of Geophysical Research: Earth Surface, 126, e2021JF006429,
907   https://doi.org/10.1029/2021JF006429, 2021.
908 Batchelor, C. L., Krawczyk, D. W., O'Brien, E., and Mulder, J.: Shelf-break glaciation and an
909   extensive ice shelf beyond northwest Greenland at the Last Glacial Maximum, Marine
910   Geology, 476, 107375, https://doi.org/10.1016/j.margeo.2024.107375, 2024.
911 Beel, C. R., Lifton, N. A., Briner, J. P., and Goehring, B. M.: Quaternary evolution and ice sheet

912   history of contrasting landscapes in Uummannaq and Sukkertoppen, western Greenland,
913   Quaternary Science Reviews, 149, 248-258,
914   https://doi.org/10.1016/j.quascirev.2016.05.033, 2016.
915 Benn, D. and Evans, D. J. A.: Glaciers and Glaciation, 2, Routledge,
916   https://doi.org/10.4324/9780203785010, 2014.
917 Bierman, P. R., Mastro, H. M., Peteet, D. M., Corbett, L. B., Steig, E. J., Halsted, C. T., Caffee,
918   M. M., Hidy, A. J., Balco, G., and Bennike, O.: Plant, insect, and fungi fossils under the
919   center of Greenland's ice sheet are evidence of ice-free times, Proceedings of the National
920   Academy of Sciences, 121, https://doi.org/10.1073/pnas.2407465121, 2024.
921 Bierman, P. R., Marsella, K. A., Patterson, C., Davis, P. T., and Caffee, M.: Mid-Pleistocene
922   cosmogenic minimum-age limits for pre-Wisconsinan glacial surfaces in southwestern
923   Minnesota and southern Baffin Island: a multiple nuclide approach, Geomorphology, 27,
924   25-39, https://doi.org/10.1016/S0169-555X(98)00088-9, 1999.
925 Bierman, P. R., Shakun, J. D., Corbett, L. B., Zimmerman, S. R., and Rood, D. H.: A persistent
926   and dynamic East Greenland Ice Sheet over the past 7.5 million years, Nature, 540, 256-
927   260, https://doi.org/10.1038/nature20147, 2016.
928 Blake, W., Boucherle, M. M., Fredskild, B., Janssens, J. A., and Smol, J. P.: The geomorphological
929   setting, glacial history and Holocene development of Kap Inglefield Sø, Inglefield Land,
930   North-West Greenland, Meddelelser om Grønland. Geoscience, 27, 1-42, 1992.
931 Briner, J. P. and Swanson, T. W.: Using inherited cosmogenic 36Cl to constrain glacial erosion
932   rates of the Cordilleran ice sheet, Geology, 26, 3-6, https://doi.org/10.1130/0091-
933   7613(1998)026<0003:UICCTC>2.3.CO;2, 1998.
934 Briner, J. P., Miller, G. H., Davis, P. T., and Finkel, R. C.: Cosmogenic radionuclides from fiord
935   landscapes support differential erosion by overriding ice sheets, Geological Society of
936   America Bulletin, 118, 406-420, https://doi.org/10.1130/B25716.1, 2006.
937 Briner, J. P., Miller, G. H., Finkel, R., and Hess, D. P.: Glacial erosion at the fjord onset zone and
938   implications for the organization of ice flow on Baffin Island, Arctic Canada,
939   Geomorphology, 97, 126-134, https://doi.org/10.1016/j.geomorph.2007.02.039, 2008.
940 Briner, J. P., Cuzzone, J. K., Badgeley, J. A., Young, N. E., Steig, E. J., Morlighem, M., Schlegel,
941   N.-J., Hakim, G. J., Schaefer, J. M., and Johnson, J. V.: Rate of mass loss from the
942   Greenland Ice Sheet will exceed Holocene values this century, Nature, 586, 70-74,
943   https://doi.org/10.1038/s41586-020-2742-6, 2020.
944 Briner, J. P., Walcott, C. K., Schaefer, J. M., Young, N. E., MacGregor, J. A., Poinar, K., Keisling,
945   B. A., Anandakrishnan, S., Albert, M. R., Kuhl, T., and Boeckmann, G.: Drill-site selection
946   for cosmogenic-nuclide exposure dating of the bed of the Greenland Ice Sheet, The
947   Cryosphere, 16, 3933-3948, 10.5194/tc-16-3933-2022, 2022.
948 Brook, E. J., Nesje, A., Lehman, S. J., Raisbeck, G. M., and Yiou, F. o.: Cosmogenic nuclide
949   exposure ages along a vertical transect in western Norway: implications for the height of
950   the Fennoscandian ice sheet, Geology, 24, 207-210, https://doi.org/10.1130/0091-
951   7613(1996)024<0207:CNEAAA>2.3.CO;2, 1996.
952 Ceperley, E. G., Marcott, S. A., Reusche, M. M., Barth, A. M., Mix, A. C., Brook, E. J., and Caffee,
953   M.: Widespread early Holocene deglaciation, Washington Land, northwest Greenland,
954   Quaternary Science Reviews, 231, 106181,
955   https://doi.org/10.1016/j.quascirev.2020.106181, 2020.
956 Christ, A. J., Bierman, P. R., Knutz, P. C., Corbett, L. B., Fosdick, J. C., Thomas, E. K., Cowling,

957   O. C., Hidy, A. J., and Caffee, M. W.: The northwestern Greenland Ice Sheet during the
958   Early Pleistocene was similar to today, Geophysical Research Letters, 47,
959   e2019GL085176, https://doi.org/10.1029/2019GL085176, 2020.
960 Christ, A. J., Bierman, P. R., Schaefer, J. M., Dahl-Jensen, D., Steffensen, J. P., Corbett, L. B.,
961   Peteet, D. M., Thomas, E. K., Steig, E. J., and Rittenour, T. M.: A multimillion-year-old
962   record of Greenland vegetation and glacial history preserved in sediment beneath 1.4 km
963   of ice at Camp Century, Proceedings of the National Academy of Sciences, 118,
964   https://doi.org/10.1073/pnas.2021442118, 2021.
965 Christ, A. J., Rittenour, T. M., Bierman, P. R., Keisling, B. A., Knutz, P. C., Thomsen, T. B.,
966   Keulen, N., Fosdick, J. C., Hemming, S. R., and Tison, J.-L.: Deglaciation of northwestern
967   Greenland during Marine Isotope Stage 11, Science, 381, 330-335,
968   10.1126/science.ade4248, 2023.
969 Colville, E. J., Carlson, A. E., Beard, B. L., Hatfield, R. G., Stoner, J. S., Reyes, A. V., and Ullman,
970   D. J.: Sr-Nd-Pb Isotope Evidence for Ice-Sheet Presence on Southern Greenland During
971   the Last Interglacial, Science, 333, 620-623, 10.1126/science.1204673, 2011.
972 Cook, S. J., Swift, D. A., Kirkbride, M. P., Knight, P. G., and Waller, R. I.: The empirical basis
973   for modelling glacial erosion rates, Nature Communications, 11, 759, 10.1038/s41467-
974   020-14583-8, 2020.
975 Corbett, L. B., Bierman, P. R., and Rood, D. H.: Constraining multi-stage exposure-burial
976   scenarios for boulders preserved beneath cold-based glacial ice in Thule, northwest
977   Greenland, Earth and Planetary Science Letters, 440, 147-157,
978   https://doi.org/10.1016/j.epsl.2016.02.004, 2016a.
979 Corbett, L. B., Bierman, P. R., and Rood, D. H.: An approach for optimizing in situ cosmogenic
980   10Be sample preparation, Quaternary Geochronology, 33, 24-34,
981   https://doi.org/10.1016/j.quageo.2016.02.001, 2016b.
982 Corbett, L. B., Bierman, P. R., Graly, J. A., Neumann, T. A., and Rood, D. H.: Constraining
983   landscape history and glacial erosivity using paired cosmogenic nuclides in Upernavik,
984   northwest Greenland, Bulletin, 125, 1539-1553, https://doi.org/10.1130/B30813.1, 2013.
985 Corbett, L. B., Bierman, P. R., Rood, D. H., Caffee, M. W., Lifton, N. A., and Woodruff, T. E.:
986   Cosmogenic 26Al/10Be surface production ratio in Greenland, Geophysical Research
987   Letters, 44, 1350-1359, https://doi.org/10.1002/2016GL071276, 2017.
988 Couette, P.-O., Lajeunesse, P., Ghienne, J.-F., Dorschel, B., Gebhardt, C., Hebbeln, D., and
989   Brouard, E.: Evidence for an extensive ice shelf in northern Baffin Bay during the Last
990   Glacial Maximum, Communications Earth & Environment, 3, 225,
991   https://doi.org/10.1038/s43247-022-00559-7, 2022.
992 Cowton, T., Nienow, P., Bartholomew, I., Sole, A., and Mair, D.: Rapid erosion beneath the
993   Greenland ice sheet, Geology, 40, 343-346, 10.1130/G32687.1, 2012.
994 Cuffey, K. M., Conway, H., Gades, A. M., Hallet, B., Lorrain, R., Severinghaus, J. P., Steig, E. J.,
995   Vaughn, B., and White, J. W. C.: Entrainment at cold glacier beds, Geology, 28, 351-354,
996   https://doi.org/10.1130/0091-7613(2000)28<351:EACGB>2.0.CO;2, 2000.
997 Cuzzone, J. K., Clark, P. U., Carlson, A. E., Ullman, D. J., Rinterknecht, V. R., Milne, G. A.,
998   Lunkka, J.-P., Wohlfarth, B., Marcott, S. A., and Caffee, M.: Final deglaciation of the
999   Scandinavian Ice Sheet and implications for the Holocene global sea-level budget, Earth
1000   and Planetary Science Letters, 448, 34-41, https://doi.org/10.1016/j.epsl.2016.05.019,
1001   2016.
1002 Daly, R. A.: The geology of the northeast coast of Labrador, Bulletin of the Museum of

Comparative Zoology at Harvard College, Geological Series, 5, 205 - 269, 1902.

de Vernal, A. and Hillaire-Marcel, C.: Natural variability of Greenland climate, vegetation, and ice volume during the past million years, Science, 320, 1622-1625, 10.1126/science.1153929, 2008.

England, J.: Coalescent Greenland and Innuitian ice during the last glacial maximum: revising the Quaternary of the Canadian High Arctic, Quaternary Science Reviews, 18, 421-456, https://doi.org/10.1016/S0277-3791(98)00070-5, 1999.

Flint, R. F.: Growth of North American Ice Sheet During the Wisconsin Age, GSA Bulletin, 54, 325-362, 10.1130/GSAB-54-325, 1943.

Goelzer, H., Nowicki, S., Payne, A., Larour, E., Seroussi, H., Lipscomb, W. H., Gregory, J., Abe-Ouchi, A., Shepherd, A., Simon, E., Agosta, C., Alexander, P., Aschwanden, A., Barthel, A., Calov, R., Chambers, C., Choi, Y., Cuzzone, J., Dumas, C., Edwards, T., Felikson, D., Fettweis, X., Golledge, N. R., Greve, R., Humbert, A., Huybrechts, P., Le clec'h, S., Lee, V., Leguy, G., Little, C., Lowry, D. P., Morlighem, M., Nias, I., Quiquet, A., Rückamp, M., Schlegel, N. J., Slater, D. A., Smith, R. S., Straneo, F., Tarasov, L., van de Wal, R., and van den Broeke, M.: The future sea-level contribution of the Greenland ice sheet: a multi-model ensemble study of ISMIP6, The Cryosphere, 14, 3071-3096, 10.5194/tc-14-3071-2020, 2020.

Goodfellow, B. W., Skelton, A., Martel, S. J., Stroeven, A. P., Jansson, K. N., and Hättestrand, C.: Controls of tor formation, Cairngorm Mountains, Scotland, Journal of Geophysical Research: Earth Surface, 119, 225-246, https://doi.org/10.1002/2013JF002862, 2014.

Gordon, J. E.: Ice-Scoured Topography and Its Relationships to Bedrock Structure and Ice Movement in Parts of Northern Scotland and West Greenland, Geografiska Annaler. Series A, Physical Geography, 63, 55-65, https://doi.org/10.2307/520564, 1981.

Gosse, J. C. and Phillips, F. M.: Terrestrial in situ cosmogenic nuclides: theory and application, Quaternary Science Reviews, 20, 1475-1560, 10.1016/s0277-3791(00)00171-2, 2001.

Hall, A. M. and Glasser, N. F.: Reconstructing the basal thermal regime of an ice stream in a landscape of selective linear erosion: Glen Avon, Cairngorm Mountains, Scotland, Boreas, 32, 191-207, https://doi.org/10.1111/j.1502-3885.2003.tb01437.x, 2003.

Hall, A. M. and Phillips, W. M.: Glacial modification of granite tors in the Cairngorms, Scotland, Journal of Quaternary Science, 21, 811-830, https://doi.org/10.1002/jqs.1003, 2006.

Hasholt, B., van As, D., Mikkelsen, A. B., Mernild, S. H., and Yde, J. C.: Observed sediment and solute transport from the Kangerlussuaq sector of the Greenland Ice Sheet (2006–2016), Arctic, Antarctic, and Alpine Research, 50, S100009, 10.1080/15230430.2018.1433789, 2018.

Hatfield, R. G., Reyes, A. V., Stoner, J. S., Carlson, A. E., Beard, B. L., Winsor, K., and Welke, B.: Interglacial responses of the southern Greenland ice sheet over the last 430,000 years determined using particle-size specific magnetic and isotopic tracers, Earth and Planetary Science Letters, 454, 225-236, https://doi.org/10.1016/j.epsl.2016.09.014, 2016.

Hogan, K. A., Dowdeswell, J. A., and Ó Cofaigh, C.: Glacimarine sedimentary processes and depositional environments in an embayment fed by West Greenland ice streams, Marine Geology, 311-314, 1-16, https://doi.org/10.1016/j.margeo.2012.04.006, 2012.

Hogan, K. A., Jakobsson, M., Mayer, L., Reilly, B. T., Jennings, A. E., Stoner, J. S., Nielsen, T., Andresen, K. J., Nørmark, E., Heirman, K. A., Kamla, E., Jerram, K., Stranne, C., and Mix, A.: Glacial sedimentation, fluxes and erosion rates associated with ice retreat in Petermann

Fjord and Nares Strait, north-west Greenland, The Cryosphere, 14, 261-286, 10.5194/tc-14-261-2020, 2020.

Hubbard, A., Bradwell, T., Golledge, N., Hall, A., Patton, H., Sugden, D., Cooper, R., and Stoker, M.: Dynamic cycles, ice streams and their impact on the extent, chronology and deglaciation of the British–Irish ice sheet, Quaternary Science Reviews, 28, 758-776, https://doi.org/10.1016/j.quascirev.2008.12.026, 2009.

Ivy-Ochs, S. and Briner, J. P.: Dating disappearing ice with cosmogenic nuclides, Elements, 10, 351-356, https://doi.org/10.2113/gselements.10.5.351, 2014.

Johnson, J. S., Woodward, J., Nesbitt, I., Winter, K., Campbell, S., Nichols, K. A., Venturelli, R. A., Braddock, S., Goehring, B. M., Hall, B., Rood, D. H., and Balco, G.: Detecting Holocene retreat and readvance in the Amundsen Sea sector of Antarctica: assessing the suitability of sites near Pine Island Glacier for subglacial bedrock drilling, EGUsphere, 2024, 1-34, 10.5194/egusphere-2024-1452, 2024.

Joughin, I. A. N., Smith, B. E., and Howat, I. M.: A complete map of Greenland ice velocity derived from satellite data collected over 20 years, Journal of Glaciology, 64, 1-11, doi:10.1017/jog.2017.73, 2018.

Khan, S. A., Choi, Y., Morlighem, M., Rignot, E., Helm, V., Humbert, A., Mouginot, J., Millan, R., Kjær, K. H., and Bjørk, A. A.: Extensive inland thinning and speed-up of Northeast Greenland Ice Stream, Nature, 611, 727-732, 10.1038/s41586-022-05301-z, 2022.

Knudsen, M. F. and Egholm, D. L.: Constraining Quaternary ice covers and erosion rates using cosmogenic 26Al/10Be nuclide concentrations, Quaternary Science Reviews, 181, 65-75, https://doi.org/10.1016/j.quascirev.2017.12.012, 2018.

Knudsen, M. F., Egholm, D. L., Jacobsen, B. H., Larsen, N. K., Jansen, J. D., Andersen, J. L., and Linge, H. C.: A multi-nuclide approach to constrain landscape evolution and past erosion rates in previously glaciated terrains, Quaternary Geochronology, 30, 100-113, https://doi.org/10.1016/j.quageo.2015.08.004, 2015.

Knutz, P. C., Newton, A. M., Hopper, J. R., Huuse, M., Gregersen, U., Sheldon, E., and Dybkjær, K.: Eleven phases of Greenland Ice Sheet shelf-edge advance over the past 2.7 million years, Nature Geoscience, 12, 361-368, https://doi.org/10.1038/s41561-019-0340-8, 2019.

Koerner, R. M.: Ice Core Evidence for Extensive Melting of the Greenland Ice Sheet in the Last Interglacial, Science, 244, 964-968, 10.1126/science.244.4907.964, 1989.

Kohl, C. P. and Nishiizumi, K.: Chemical isolation of quartz for measurement of in-situ-produced cosmogenic nuclides, Geochimica et Cosmochimica Acta, 56, 3583-3587, https://doi.org/10.1016/0016-7037(92)90401-4, 1992.

Kokfelt, T. F., Willerslev, E., Bjerager, M., Heijboer, T., Keulen, N., Larsen, L. M., Pedersen, C. B., Pedersen, M., Svennevig, K., Sønderholm, M., Walentin, K. T., and Weng, W. L.: Seamless digital 1:500 000 scale geological map of Greenland, version 2.0 (V1), GEUS Dataverse [dataset], doi:10.22008/FK2/FWX5ET, 2023.

Koppes, M., Hallet, B., Rignot, E., Mouginot, J., Wellner, J. S., and Boldt, K.: Observed latitudinal variations in erosion as a function of glacier dynamics, Nature, 526, 100-103, 10.1038/nature15385, 2015.

Koppes, M. N. and Montgomery, D. R.: The relative efficacy of fluvial and glacial erosion over modern to orogenic timescales, Nature Geoscience, 2, 644-647, 10.1038/ngeo616, 2009.

Korschinek, G., Bergmaier, A., Faestermann, T., Gerstmann, U. C., Knie, K., Rugel, G., Wallner, A., Dillmann, I., Dollinger, G., von Gostomski, C. L., Kossert, K., Maiti, M., Poutivtsev, M., and Remmert, A.: A new value for the half-life of 10Be by Heavy-Ion Elastic Recoil

Detection and liquid scintillation counting, Nuclear Instruments and Methods in Physics Research Section B: Beam Interactions with Materials and Atoms, 268, 187-191, https://doi.org/10.1016/j.nimb.2009.09.020, 2010.

Korsgaard, N. J., Nuth, C., Khan, S. A., Kjeldsen, K. K., Bjørk, A. A., Schomacker, A., and Kjær, K. H.: Digital elevation model and orthophotographs of Greenland based on aerial photographs from 1978–1987, Scientific Data, 3, 1-15, https://doi.org/10.1038/sdata.2016.32, 2016.

Krabbendam, M. and Bradwell, T.: Quaternary evolution of glaciated gneiss terrains: pre-glacial weathering vs. glacial erosion, Quaternary Science Reviews, 95, 20-42, https://doi.org/10.1016/j.quascirev.2014.03.013, 2014.

Lal, D.: Cosmic ray labeling of erosion surfaces: in situ nuclide production rates and erosion models, Earth and Planetary Science Letters, 104, 424-439, https://doi.org/10.1016/0012-821X(91)90220-C, 1991.

LeBlanc, D. E., Shakun, J. D., Corbett, L. B., Bierman, P. R., Caffee, M. W., and Hidy, A. J.: Laurentide Ice Sheet persistence during Pleistocene interglacials, Geology, 51, 496-499, 10.1130/G50820.1, 2023.

Lisiecki, L. E. and Raymo, M. E.: A Pliocene-Pleistocene stack of 57 globally distributed benthic δ18O records, Paleoceanography, 20, https://doi.org/10.1029/2004PA001071, 2005.

MacGregor, J. A., Chu, W., Colgan, W. T., Fahnestock, M. A., Felikson, D., Karlsson, N. B., Nowicki, S. M. J., and Studinger, M.: GBaTSv2: A revised synthesis of the likely basal thermal state of the Greenland Ice Sheet, The Cryosphere Discuss., 2022, 1-25, 10.5194/tc-2022-40, 2022.

Margold, M., Stokes, C. R., and Clark, C. D.: Ice streams in the Laurentide Ice Sheet: Identification, characteristics and comparison to modern ice sheets, Earth-Science Reviews, 143, 117-146, https://doi.org/10.1016/j.earscirev.2015.01.011, 2015.

Margold, M., Stokes, C. R., and Clark, C. D.: Reconciling records of ice streaming and ice margin retreat to produce a palaeogeographic reconstruction of the deglaciation of the Laurentide Ice Sheet, Quaternary Science Reviews, 189, 1-30, https://doi.org/10.1016/j.quascirev.2018.03.013, 2018.

Margreth, A., Gosse, J. C., and Dyke, A. S.: Quantification of subaerial and episodic subglacial erosion rates on high latitude upland plateaus: Cumberland Peninsula, Baffin Island, Arctic Canada, Quaternary Science Reviews, 133, 108-129, https://doi.org/10.1016/j.quascirev.2015.12.017, 2016.

Marrero, S. M., Hein, A. S., Naylor, M., Attal, M., Shanks, R., Winter, K., Woodward, J., Dunning, S., Westoby, M., and Sugden, D.: Controls on subaerial erosion rates in Antarctica, Earth and Planetary Science Letters, 501, 56-66, https://doi.org/10.1016/j.epsl.2018.08.018, 2018.

Mason, O. K.: Beach ridge geomorphology at Cape Grinnell, northern Greenland: a less icy Arctic in the mid-Holocene, Geografisk Tidsskrift-Danish Journal of Geography, 110, 337-355, https://doi.org/10.1080/00167223.2010.10669515, 2010.

Miller, G. H., Briner, J. P., Lifton, N. A., and Finkel, R. C.: Limited ice-sheet erosion and complex exposure histories derived from in situ cosmogenic 10Be, 26Al, and 14C on Baffin Island, Arctic Canada, Quaternary Geochronology, 1, 74-85, https://doi.org/10.1016/j.quageo.2006.06.011, 2006.

Mouginot, J., Rignot, E., Scheuchl, B., Fenty, I., Khazendar, A., Morlighem, M., Buzzi, A., and

1139   Paden, J.: Fast retreat of Zachariæ Isstrøm, northeast Greenland, Science, 350, 1357-1361,
1140   10.1126/science.aac7111, 2015.
1141 Nichols, R. L.: Geomorphology of Inglefield land, north Greenland, Meddelelser om Grønland,
1142   188, 3-105, 1969.
1143 Nishiizumi, K.: Preparation of 26Al AMS standards, Nuclear Instruments and Methods in Physics
1144   Research Section B: Beam Interactions with Materials and Atoms, 223-224, 388-392,
1145   https://doi.org/10.1016/j.nimb.2004.04.075, 2004.
1146 Nishiizumi, K., Imamura, M., Caffee, M. W., Southon, J. R., Finkel, R. C., and McAninch, J.:
1147   Absolute calibration of 10Be AMS standards, Nuclear Instruments and Methods in Physics
1148   Research Section B: Beam Interactions with Materials and Atoms, 258, 403-413,
1149   https://doi.org/10.1016/j.nimb.2007.01.297, 2007.
1150 Patton, H., Hubbard, A., Andreassen, K., Auriac, A., Whitehouse, P. L., Stroeven, A. P.,
1151   Shackleton, C., Winsborrow, M., Heyman, J., and Hall, A. M.: Deglaciation of the Eurasian
1152   ice sheet complex, Quaternary Science Reviews, 169, 148-172,
1153   https://doi.org/10.1016/j.quascirev.2017.05.019, 2017.
1154 Phillips, W. M., Hall, A. M., Mottram, R., Fifield, L. K., and Sugden, D. E.: Cosmogenic 10Be
1155   and 26Al exposure ages of tors and erratics, Cairngorm Mountains, Scotland: Timescales
1156   for the development of a classic landscape of selective linear glacial erosion,
1157   Geomorphology, 73, 222-245, https://doi.org/10.1016/j.geomorph.2005.06.009, 2006.
1158 Portenga, E. W. and Bierman, P. R.: Understanding Earth's eroding surface with 10 Be, GSA
1159   Today, 21, 6, 10.1130/G111A.1, 2011.
1160 Reyes, A. V., Carlson, A. E., Beard, B. L., Hatfield, R. G., Stoner, J. S., Winsor, K., Welke, B.,
1161   and Ullman, D. J.: South Greenland ice-sheet collapse during marine isotope stage 11,
1162   Nature, 510, 525-528, https://doi.org/10.1038/nature13456, 2014.
1163 Roberts, D. H., Rea, B. R., Lane, T. P., Schnabel, C., and Rodés, A.: New constraints on Greenland
1164   ice sheet dynamics during the last glacial cycle: evidence from the Uummannaq ice stream
1165   system, Journal of Geophysical Research: Earth Surface, 118, 519-541,
1166   https://doi.org/10.1002/jgrf.20032, 2013.
1167 Sbarra, C. M., Briner, J. P., Graham, B. L., Poinar, K., Thomas, E. K., and Young, N. E.: Evidence
1168   for a more extensive Greenland Ice Sheet in southwestern Greenland during the Last
1169   Glacial Maximum, Geosphere, https://doi.org/10.1130/GES02432.1, 2022.
1170 Schaefer, J. M., Finkel, R. C., Balco, G., Alley, R. B., Caffee, M. W., Briner, J. P., Young, N. E.,
1171   Gow, A. J., and Schwartz, R.: Greenland was nearly ice-free for extended periods during
1172   the Pleistocene, Nature, 540, 252-255, https://doi.org/10.1038/nature20146, 2016.
1173 Skov, D. S., Andersen, J. L., Olsen, J., Jacobsen, B. H., Knudsen, M. F., Jansen, J. D., Larsen, N.
1174   K., and Egholm, D. L.: Constraints from cosmogenic nuclides on the glaciation and erosion
1175   history of Dove Bugt, northeast Greenland, GSA Bulletin, 132, 2282-2294,
1176   10.1130/B35410.1, 2020.
1177 Skyttä, P., Nordbäck, N., Ojala, A., Putkinen, N., Aaltonen, I., Engström, J., Mattila, J., and
1178   Ovaskainen, N.: The interplay of bedrock fractures and glacial erosion in defining the
1179   present-day land surface topography in mesoscopically isotropic crystalline rocks, Earth
1180   Surface Processes and Landforms, https://doi.org/10.1002/esp.5596, 2023.
1181 Søndergaard, A. S., Larsen, N. K., Steinemann, O., Olsen, J., Funder, S., Egholm, D. L., and Kjær,
1182   K. H.: Glacial history of Inglefield Land, north Greenland from combined in situ 10 Be
1183   and 14 C exposure dating, Climate of the Past, 16, 1999-2015, https://doi.org/10.5194/cp-
1184   16-1999-2020, 2020.

Spector, P., Stone, J., Pollard, D., Hillebrand, T., Lewis, C., and Gombiner, J.: West Antarctic sites for subglacial drilling to test for past ice-sheet collapse, The Cryosphere, 12, 2741-2757, https://doi.org/10.5194/tc-12-2741-2018, 2018.

Spotila, J. A., Buscher, J. T., Meigs, A. J., and Reiners, P. W.: Long-term glacial erosion of active mountain belts: Example of the Chugach–St. Elias Range, Alaska, Geology, 32, 501-504, https://doi.org/10.1130/G20343.1, 2004.

Stone, J. O.: Air pressure and cosmogenic isotope production, Journal of Geophysical Research: Solid Earth, 105, 23753-23759, https://doi.org/10.1029/2000JB900181, 2000.

Strunk, A., Knudsen, M. F., Egholm, D. L., Jansen, J. D., Levy, L. B., Jacobsen, B. H., and Larsen, N. K.: One million years of glaciation and denudation history in west Greenland, Nature communications, 8, 1-8, https://doi.org/10.1038/ncomms14199, 2017.

Sugden, D. E.: Landscapes of glacial erosion in Greenland and their relationship to ice, topographic and bedrock conditions, Institute of British Geographers Special Publication, 7, 177-195, 1974.

Sugden, D. E.: Glacial Erosion by the Laurentide Ice Sheet, Journal of Glaciology, 20, 367-391, 10.3189/S0022143000013915, 1978.

Sugden, D. E., Balco, G., Cowdery, S. G., Stone, J. O., and Sass, L. C.: Selective glacial erosion and weathering zones in the coastal mountains of Marie Byrd Land, Antarctica, Geomorphology, 67, 317-334, https://doi.org/10.1016/j.geomorph.2004.10.007, 2005.

Syvitski, J. P. M., Andrews, J. T., and Dowdeswell, J. A.: Sediment deposition in an iceberg-dominated glacimarine environment, East Greenland: basin fill implications, Global and Planetary Change, 12, 251-270, https://doi.org/10.1016/0921-8181(95)00023-2, 1996.

Ugelvig, S. V. and Egholm, D. L.: The influence of basal-ice debris on patterns and rates of glacial erosion, Earth and Planetary Science Letters, 490, 110-121, https://doi.org/10.1016/j.epsl.2018.03.022, 2018.

Young, N. E., Schaefer, J. M., Briner, J. P., and Goehring, B. M.: A 10Be production-rate calibration for the Arctic, Journal of Quaternary Science, 28, 515-526, https://doi.org/10.1002/jqs.2642, 2013.

Young, N. E., Lesnek, A. J., Cuzzone, J. K., Briner, J. P., Badgeley, J. A., Balter-Kennedy, A., Graham, B. L., Cluett, A., Lamp, J. L., Schwartz, R., Tuna, T., Bard, E., Caffee, M. W., Zimmerman, S. R. H., and Schaefer, J. M.: In situ cosmogenic 10Be–14C–26Al measurements from recently deglaciated bedrock as a new tool to decipher changes in Greenland Ice Sheet size, Clim. Past, 17, 419-450, 10.5194/cp-17-419-2021, 2021.